Large Eddy Simulation of turbulent combustion in a stagnation point reverse flow combustor using detailed chemistry

CrossMark

C. Duwig *, P. Iudiciani [1]

Division of Fluid Mechanics, Lund University, SE-22100 Lund, Sweden

HIGHLIGHTS

- We model flameless combustion with complex chemistry and LES.
- A comprehensive sensitivity analysis of the results is presented.
- Large scale rotational and helical modes are identified.
- The reaction layer structure is presented including intermediate species.
- Recommendations are given on which species to follow during flameless combustion.

ARTICLE INFO

ABSTRACT

For meeting stringent emission restrictions, a modern solution is to operate in or close to the flameless mode. It implies a copious dilution of the reactants with vitiated gas resulting in low oxidant or fuel concentration and consequently low volumetric heat-release rate. On the contrary to traditional flames where heat release is occurring in very thin fronts, the flameless operation lies in the distributed reaction regime. Flameless operation is therefore associated with complex and non-linear interaction between mixing and chemical reactions. In this framework, this paper investigates turbulent combustion in a stagnation point reverse flow combustor and presents one of the first studies combining Large Eddy Simulation and detailed chemistry for capturing the reaction and flow dynamics during flameless combustion. The paper reports a comprehensive sensitivity analysis where the effects of the numerical discretization grid, of the chemical mechanism, of the operation (premixed vs. non-premixed) and of the heat-losses at the walls are studied and compared. Further, the simulation results are compared with experimental data from the literature, giving confidence in the quality of the predictions. The reaction and flow dynamics are extracted from the results using modal analysis, showing rotational and helical structures. Finally, the distribution of intermediate species in the reaction layer is investigated bringing some new insights into the flameless combustion process and providing recommendations for further experimental investigations.

1. Introduction

Despite more than 60 years of research, turbulent combustion still poses considerable challenges [1]. The interaction between turbulent structures and chemical reactions features a multi-scale non-linear problem. In the limit of a very thin, or even infinitely thin, reaction layer, the flamelet concept has been successful. For example, typical low Reynolds number (*Re*) laboratory scale experiments often fall in the flamelet regime and have led to numerous studies and successful modeling activities [1,2]. However, this regime is not always relevant to industrial combustion devices which commonly operate at very high *Re* in the distributed combustion regime (high Karlovitz number – *Ka*).

A modern solution to avoid NO_x/soot formation (and unwanted peak temperatures) consists of diluting the reactants with large amount of inert gases. Practically, this can be done by using low calorific value fuels, dilution by massive injection of steam or intensive exhaust gas recirculation (EGR). Operating with low local oxygen concentration ensures that the fuel combustion is only complete when the fuel jet is mixed with a copious amount of inert

---

* Corresponding author. Address: Division of Fluid Mechanics, Dept. Energy Sciences, Box 118, Lund University, Faculty of Engineering (LTH), SE-22100 Lund, Sweden. Tel.: +46 46 222 3184; fax: +46 46 222 4717.
E-mail address: Christophe.Duwig@energy.lth.se (C. Duwig).
[1] Present address: Lloyd's Register ODS, 2900 Hellerup, Denmark.

gases. Under oxygen depleted conditions, the reaction rate is considerably lowered by the dilution and the reaction zone expands over a significant fraction of the combustor volume [3–5] – unlike traditional thin flame fronts. This technique is frequently referred to as MILD (Moderate or Intense Low oxygen Dilution). Although the MILD operation is popular [3–9] and successful, one may also consider very lean combustion (with significant preheat) which presents the same characteristics in terms of low intensity and distributed reactions. Such operation is without intense light emission and could be referred to as flameless combustion [10–15]. In all cases, one needs to find the right balance between reactant dilution and preheating to maintain complete combustion. A common solution is to ensure that the fresh reactants entrain a large amount of flue gases with a mixing time scale much shorter than the corresponding chemical time scale. In other words, the intention is to mix fast enough so that chemical reactions cannot take place before a given level of dilution is achieved.

Engineering examples of furnaces operating in MILD regime are found in the literature, e.g. [7–9]. However, there are no industrial gas turbine combustors operating in the MILD or flameless regime reported in the literature. The main difficulty lies in the available space for adding additional devices, the operating conditions (lean combustion) as well as the impossibility of heat-removal. In fact, gas turbine and aero-engines typically operate fuel lean (high oxygen content) adiabatic combustion which rules out MILD operation. Pioneering works including high-speed jet combustors [10,15] have shown promising results for adapting flameless technology to gas turbine applications. Similar work on Stagnation Point Reverse Flow (SPRF) combustor [12–14] are also promising, although it was not shown yet that the SPRF operates in the flameless regime. However, these activities are limited by the lack of theoretical understanding of the driving mechanism of flameless combustion. High Ka combustion in general is not well understood and has not been investigated extensively. There is therefore a need for detailed investigation of flameless/high Ka operation. In particular, pioneer work [14] has shown the importance of finite rate chemistry for this combustion regime, highlighting the need of studies accounting for detailed chemistry effects.

One may express the challenge recalling the non-linear and multi-scale nature of turbulence and turbulent combustion. When focussing on high Ka problems, the characteristic time scale ranges of the chemical oxidation and of the turbulent mixing overlap significantly. The interaction between a wide range of turbulent scales and the chemical reaction front are intimate. It differs significantly from the flamelet regime where scale-separation is valid. Considering high Ka operation, flame stabilisation is secured using recirculation of vitiated gases – using the hot gases to dilute the reactants and promoting robust initial reactions. Entrainment of vitiated gases demands a configuration where the fresh reactant and the hot combustion product streams have different velocities. This results in an interface between the two streams that is subject to shear-layer instabilities. This shear layer may promote turbulence – preferably high turbulence levels in the shear layer can also lead to rapid mixing. Fresh and vitiated gases are mixed with little reaction locally, whilst downstream (if the strain rate is sufficiently reduced and there is no significant heat loss) the oxidation reaction can proceed. Capturing and modeling the interaction between chemical oxidation and turbulence in the shear-layer is of vital importance in order to predict the operation performances and stability limits correctly.

To that end, experiments have been conducted to collect valuable information – featuring a high-speed jet issuing into a hot co-flow, e.g. [11,16–22]. Among these, recent high Ka experiments including the (Piloted) Premixed Jet Burner [21–24] have been well characterized thanks to advanced laser diagnostics and numerical simulations using detailed chemistry. Although it features a simple academic test case, it is suitable to evaluate modeling approaches and is relevant for modeling fuel lean combustors. In fact, Refs. [14,23,24] showed the importance of the finite rate chemistry modeling and highlighted the thick reaction layer – thick enough to be resolved on a reasonable Large Eddy Simulation grid [23,24]. Another burner, the SPRF [12–14] combustor, features a very similar combustion problem with a lean premixed jet (equivalence ratio close to 0.6) entraining a large amount of product gases. It constitutes a strong ground for realistic studies of combustion under flameless (or flameless-like) conditions. However, to date, only global chemistry simulations of the SPRF have been reported [14]. There is therefore a need to undertake more detailed studies of the SPRF, capturing several intermediate and radical species concentrations, in order to understand the oxidation reactions sequence and combustion process.

The aim of the present contribution is twofold: (i) identify the important simulation parameters via a sensitivity analysis, and (ii) monitor intermediate species in the reaction zone for understanding the reaction sequence. To that end, our strategy is to use an approach combining Large Eddy Simulation and detailed chemistry [23] for modeling the SPRF and to investigate further the combustion process at high-Ka. The present paper proceeds as follows; firstly, the modeling approach is presented and discussed critically. Secondly, the combustor geometry and experimental database are presented followed by the presentation of the numerical simulation. Finally, the results are presented including a sensitivity analysis and novel understanding of the combustion process.

2. Modeling for the SPRF combustor

Many practical combustion devices operate at high Reynolds numbers with intense anisotropic turbulence. Poinsot and Veynante [2] summarize the different alternatives for turbulence modeling and highlight the superiority of Large Eddy Simulation (LES) over both Reynolds Averaged Navier Stokes (RANS) techniques (in terms of accuracy) and Direct Numerical Simulation (in terms of ability to handle realistic combustors). Large Eddy Simulation has been shown to be an effective approach for handling flows that feature unsteady coherent structures, such as in combustors [2,14,23], and LES is utilized in the present work. There are, however, two open key issues related to LES that must be addressed. Firstly, a subgrid scale (SGS) models must be employed in the momentum and energy equations. This is in addition to the equations related to species transport and equation of state that are required to close the system. Secondly, closing the species transport equations involves finding a suitable reaction mechanism to describe fuel combustion.

Focusing on the limit $Ka \gg 1$, the turbulent eddies are smaller than the reaction layers and penetrate the flame front. This results an intense small scale mixing with vitiated gases being mixed with fresh gases. This is referred to as the 'well-stirred reactor' or 'distributed reaction' regime since the reaction zone is not a thin sheet anymore and may be described as a collection of well- or partially-stirred reactors.

2.1. Governing equations

The basic equations describing the motion of a fluid are the transport of momentum, species, and energy. The system of equations has to be closed with an equation of state. When the species undergo exo- or endo-thermal chemical reactions, one has to add source/sink terms to the species transport equations and the energy equation. If the characteristic speed of the fluid is considerably smaller than the speed of sound, one may decouple the

acoustical effects from the flow, which simplifies the system of equations (low Mach-number formulation). Under this assumption, the density is function of temperature and gas composition only. In LES, the dependent variables are filtered and one introduces the density weighed filtering, $\tilde{f} = \overline{\rho f}/\bar{\rho}$ where overbars denote spatial filtering, e.g. [2]. Applying the filtering to the reactive Navier–Stokes Equations and the state equation yields:

$$\begin{cases} \partial_t \overline{\rho} + \nabla \cdot (\overline{\rho u}) = 0, \\ \partial_t \bar{\rho} \tilde{Y}_i + \nabla \overline{\rho u} \tilde{Y}_i = \nabla \cdot (\overline{\rho u} \tilde{Y}_i - \overline{\rho u Y_i} + \rho D_i \nabla \tilde{Y}_i) + \overline{\dot{w}}_i, i = 1, \ldots, N, \\ \partial_t \bar{\rho} \tilde{u} + \nabla \overline{\rho u} \tilde{u} = -\nabla \bar{p} + \nabla \cdot (\overline{\rho u} \tilde{u} - \overline{\rho u u} + \sigma), \\ \partial_t \bar{\rho} \tilde{h} + \nabla \overline{\rho u} \tilde{h} = \nabla \cdot (\overline{\rho u} \tilde{h} - \overline{\rho u h} + \lambda \nabla \tilde{T}), \\ \overline{\rho} = \overline{\left(\frac{p_0}{RT}\right)} \end{cases}$$

(1)

where u is the velocity vector, h the total enthalpy, p_0 the reference pressure, ρ the density, σ the viscous contribution, λ the thermal conductivity, R the specific ideal gas constant, D_i the diffusivity of species i, Y_i the mass fraction of species i and $\overline{\dot{w}}_i$ the reaction term of species i. The species diffusion is described by Fick's law. The mixture viscosity is modeled by Sutherland's law and the thermal conduction is modeled similarly [23]. The transport subgrid terms arising on the right-hand-side in equations (1_{1-4}) are modeled using a classical gradient type with an effective 'eddy' viscosity computed using the classical Smagorinky model [2]. We use here the analogy between the unresolved transport of momentum and scalar and extend the effective viscosity for computing the effective diffusivity and conductivity using effective Schmidt and Prandtl numbers taken to be $Sc_\Delta = 1$ and $Pr_\Delta = 1$ respectively [2,23].

2.2. Chemical mechanism

Incorporating combustion chemistry into LES involves finding a suitable reaction mechanism and solving the filtered species equations (1_2). For methane combustion, comprehensive chemical kinetics mechanisms can potentially involve hundreds of species and thousands of reactions. It could be computationally prohibitive in a three dimensional Eulerian framework to resolve hundreds of additional species transport equations, therefore some simplification, hence modeling of the unresolved kinetics, must be employed.

Very few LES studies use relatively detailed chemistry (skeletal mechanisms), e.g. [23,25,26], and a part of the present study will report a sensitivity analysis to the choice of the oxidation scheme. At this point one may mention tabulated chemistry [24,27–32] as an alternative to chemical schemes where complex chemical information is stored in lookup tables in a compact format. This solution has been proven successful in few simple cases e.g. [24,27–32] but cannot address any combustion problem yet. A particular difficult issue lies in including the heat-losses [32] in the tabulation chemistry as well as accounting for several fuels and oxidants. To that respect, using chemical schemes giving Arrhenius reaction rate is a pragmatic choice for the present simulations.

We consider three methane oxidation schemes with increasing number of species. Firstly, a 7-species (CH_4, CO, H_2, O_2, CO_2, H_2O, N_2), 4-step global mechanism by Jones and Lindstedt [33] (also referred to as J&L in the following) is considered. In fact, the use of a global mechanism was shown to simulate the heat fluxes in some other MILD burner, e.g. [34]. This short global mechanism enables rapid simulations without significant additional cost related to species transport. It is a first choice but its performance needs to be compared with more costly alternatives. Further, the skeletal mechanism DRM22 [35] (23 species, 104 reactions) and Warnatz's methane oxidation mechanism (34 species, 164 reactions) [36,37] are used to account for radicals. The importance of finite rate

chemistry for the SPRF was highlighted in [14] while the need for detailed chemistry when simulating MILD combustion is also well known [38–40]. In the Reynolds Averaged Navier–Stokes framework, Christo and Dally [38] showed the potential of using GRI [41] as chemical scheme for MILD combustion. Further, Galletti et al. [39] investigated the GRI against the skeletal mechanism (DRM [35]) noting few differences. Comparing different skeletal mechanisms, Aminian et al. [40] pointed out the importance of C2 species – although the fuel contained only methane. They analyzed the different paths for C_2H_2 consumption and pointed out a limitation of the DRM22 not considering HCCO, hence the route $C_2H_2 + O \rightarrow HCCO + H$. Although these studies relate to MILD combustion – locally fuel rich conditions while the SPRF operates fuel lean [14] – they highlighted the importance of assessing the impact of different oxidation routes in *flameless* combustion. Therefore, we consider both a skeletal mechanism including C_2 species (DRM22) as well as an established methane oxidation mechanism with a more comprehensive treatment of the C_2 chemistry (here the mechanism by Warnatz – abbreviated as Warn. in some Figures). In addition, DRM22 is based on GRI1.2 which did not cover the low temperature reactions well and it is therefore important to check against a more comprehensive mechanism, here by Warnatz.

A freely propagating premixed laminar flame will be used as reference in the following; it was computed using Cantera [42] together with Warnatz's methane oxidation mechanism. We note that similar simulation using GRI or DRM22 provided very similar output in terms of flame speed, flame thickness, CO and OH profiles.

2.3. Subgrid scale modeling

An additional modeling issue lies in the species equations (1_2) which contain the filtered reaction rates, $\overline{\dot{w}}_i$. The reaction rates are non-linear functions of the species concentration and the temperature. Different avenues were followed for modeling of the filtered reaction rate, historically starting by extending Reynolds Averaged Navier–Stokes (RANS) combustion models to LES applications. Recently modern methods were proposed that were specifically designed for the LES framework [2]. Examples of such methods includes (i) Implicit LES (ILES) [23,24,43], (ii) Thickened Flame Models (TFM) [44], (iii) Linear Eddy Models (LEM), with embedded 1D grids [14,25], (iv) Flamelet Models (FM) [28,29,45,46], (v) Eddy Dissipation Concept (EDC) [47], (vi) Partially Stirred Reactor (PaSR) [48,49] and (vii) Filtered Density Function (FDF) models [31,50,26]. We note here that if methods (iv–vi) have a counter-part in the RANS framework, methods (i–iii) are solely valid for LES applications.

The flame of present interest is characterized by a relatively high Karlovitz number and designed to highlight finite rate chemistry effects. Suitable models might then be ILES, TFM, LEM, EDC, PaSR and FDF, hence ruling out FM models. This choice is supported by a previous study [14] showing the inadequacy of flamelet approaches for modeling the SPRF. At this point, we can cite recent progresses using unsteady or interactive flamelet closures which extend the approaches to MILD regime [51].

Based on [14], one can retain the LEM and TFM. Not surprisingly, these models enable to capture finite rate chemistry and solve Arrhenius reaction rates on the fly and model naturally the influence of heat-losses on the flame. In fact ILES, EDC and PaSR have interlinks with TFM and are also candidates. In the present study, we aim at using several oxidation schemes with increasing number of species and focus on using ILES while discussions upon the differences between ILES, TFM and PaSR will follow.

For a species j, the ILES (also referred to sometimes as Monotonically Integrated LES – MILES) closure gives [23,24,43]:

$$\overline{\dot{w}(Y_i, T)} = \dot{w}_j(\tilde{Y}_i, \tilde{T})$$

(2)

where the reaction rate is obtained from an Arrhenius expression. We should highlight here that relation (2) would fail in the RANS framework but is valid for laminar flow simulation and direct numerical simulation (DNS). LES being an intermediate between RANS and DNS, the validity of (2) would depend on the relative grid resolution and on the subgrid physics. If the grid resolution is close to DNS and the reacting layer is adequately resolved, equation (2) is valid. Although using a typical LES-grid (i.e. far from DNS), relation (2) may approximate the reaction rate reasonably well as reported in [23,24,43]. In other words, a very intense subgrid mixing ensures that a perfectly stirred reactor can reasonably represent the filter box (or LES grid cell) and subgrid concentration and temperature are close to be homogeneous. It also implies that the intense subgrid mixing acts faster than any chemical reaction. One may quantify the competition between both processes using a local Damköhler number Da_Δ comparing the chemical and large subgrid structure characteristic time scales, $\tau_c \sim \delta_L/S_L$ (laminar flame thickness/laminar flame speed) and $\tau_\Delta \sim \Delta/u_\Delta$ (filter size/subgrid velocity fluctuation) respectively, giving:

$$Da_\Delta = \frac{\tau_\Delta}{\tau_c} = \frac{\Delta}{\delta_L} \cdot \frac{S_L}{u_\Delta} \tag{3}$$

Da_Δ decreases with decreasing Δ. For *large* Δ so that $Da_\Delta > 1$), the filter box is segregated with gradients of temperature and species. For *small* Δ so that $Da_\Delta < 1$), the filter box is well stirred and homogeneous when it comes to temperature and species concentrations. Hence, $Da_\Delta < 1$ is a criterion for addressing the validity of ILES. It follows that PaSR and TFM models relates to Da_Δ and include an estimation of the subgrid scale segregation between reacting and non-reacting fractions (hence an estimation of the subgrid scalar gradients). For example, the subgrid fraction of reacting mixture κ in PaSR [48,49] is expressed as function of the subgrid mixing and chemical time scales and reads:

$$K = \frac{1}{1 + \tau_\Delta \tau_c} = \frac{1}{1 + Da_\Delta} \tag{4}$$

In the limit of $Da_\Delta \ll 1$ (well stirred subgrid filter box), the PaSR model recovers the ILES closure. The thickening factor F in the TFM [44] ensures that there are not subgrid scalar gradients (the front is resolved on the LES grid), giving:

$$F = k\frac{\Delta}{\delta} \sim k\frac{\Delta}{\delta_L} = k\frac{u_\Delta}{S_L}Da_\Delta \sim k(\Xi - 1)Da_\Delta \tag{5}$$

where k is the number of LES cells resolving the scalar gradients (typically 3–5), δ the thickness of the un-thickened scalar front and Ξ is the subgrid flame wrinkling.

Da_Δ is indeed an indicator of the validity of the ILES assumption, and we estimate using (4) that a subgrid segregation $\kappa > 0.9$ (nearly homogeneous subgrid field) corresponds to $Da_\Delta < 0.1$. Alternatively, ILES is the limit of the TFM at $F < 1$ giving $Da_\Delta < 0.17$ with $k \sim 3$ and $\Xi \sim 3$. In the following, we use F as indicator, keeping in mind the interlinks with the two other non-dimensional numbers.

An important remark lies in the estimation of the chemical time scales for estimation of Da and Ka. The chemical time scale is traditionally extracted from laminar freely propagating flames (and we follow this procedure presently) but it is unclear if this estimation is close when dealing with distributed reactions. In fact, the interaction with turbulence impacts highly on the reaction rates by diluting the reactants and increasing the local temperature – both having conflicting effect on Da and Ka. In absence of an alternative procedure, we should keep in mind this limitation when discussing the combustion regime.

3. Presentation of the SPRF

The SPRF [12–14] features a co-axial injector discharging into a cylinder. The cylinder acts as combustion chamber and has a diameter and length of $D = 0.07$ m and $L = 0.308$ m, respectively in [14] while it is slightly different in [12,13] (not considered presently). The end of the cylinder in the streamwise direction is closed with only one outlet surrounding the injector. The dimensions are given in [14]. The injector consists of a central round fuel injector of diameter 0.0041 m surrounded by an air injection annulus (inner diameter 0.00635 m – outer diameter $d = 0.0125$ m). The combustor outlet features an annulus of inner diameter 0.01645 m and outer diameter 0.07 m. Solid walls fill the gap between the fuel and air injector and between the air injector and the outlet annulus. Fig. 1 shows the combustor and injectors. The general flow field includes a central jet ending at a stagnation point where the flow reverts and returns to the injection plane where it exits the combustor [12–14]. When the combustor is filled with hot-burnt gases, the fresh incoming gases are in contact with out-going burnt gases. The originality of the device lies in the strong shear between the incoming cold flow and the out-going hot gases. The configuration resembles a Jet in a Counter-Flow (JiCoF) [52,53], except the confinement caused by the walls. Compared to a jet in a coflow, the JiCoF exhibits higher turbulence level and much shorter jet core length. The reverse flow configuration makes the jet globally unstable [53], explaining the intense mixing – even at low and moderate Reynolds numbers [52]. Isothermal unconfined flow experiments [52] and simulations [53] evidenced the intense large-scale dynamics including a large precessing motion of the jet core with benefits in terms of rapid mixing of the jet core. These elements make the SPRF an efficient configuration enabling the rapid mixing of the incoming fresh gas with copious amount of flue gas. Further, they also support the choice of LES as RANS is known to fail capturing the mixing resulting from large and energetic coherent structures.

Two configurations are of present interest. They correspond to two operation modes of the SPRF [14], namely non-premixed operation (NPO) with the fuel injected in the center injector and the premixed operation (PO) where the fuel is mixed with air prior to injection. During PO, the inner/fuel nozzle is not discharging gas into the combustor. Fig. 1 illustrates the fuel/air mixing and the location of the burnt gases showing mixture fraction field and temperature iso-line $T = 1000$ K for NPO.

We focus on the operating conditions presented in [14] showing good performance in terms of flame stability and low emissions. The corresponding air flow is 8.1 g/s. The global fuel/air equivalence ratio is 0.58 for the PO and 0.54 for the NPO. The slight difference in equivalence ration results in slightly lower temperatures in the NPO case but no strong difference as the operation is far from lean-blow-off. This difference is still to be kept in mind when comparing PO and NPO.

The air is slightly preheated while passing in the feeding pipe before entering the combustion chamber. The power density of the case is 13.3 MW/m^3 with total thermal power of 15.8 kW.

The corresponding chemical time scale for a freely propagating premixed flame (methane/air – $\Phi = 0.58$, unburnt temperature 500 K [14]) would be $\tau_c = \delta_L/S_L = 0.0016$ s with a chemical length scale based on the thermal thickness $\delta_L = 0.0006$ m. The jet time scale based on the air annular width h and the air bulk velocity is $\tau \sim h/U_a = 5 \times 10^{-5}$ s. The global Damköhler and Karlovitz numbers reads $Da = \tau/\tau_c \sim 3 \times 10^{-2}$ and $Ka \sim (TI * U_a/S_L)^{1.5}(\delta_L/h)^{0.5} \sim 110$, respectively. Here, TI is the turbulence intensity estimated to be around 0.15. The Reynolds number based on h and the airflow is $Re \sim 12900$. We note further that the integral length scale h is only ten times larger than the laminar flame thickness. In
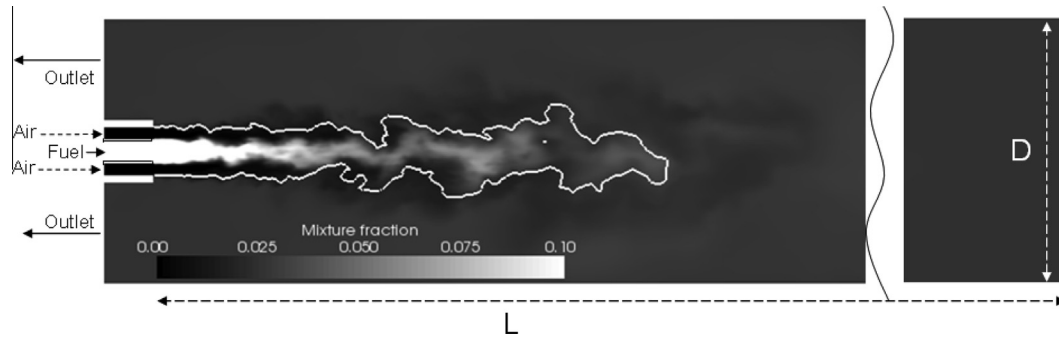
Fig. 1. Randomly chosen mixture fraction snapshot indicating the fuel and air injection at NPO. The white line corresponds to the temperature iso-level $T = 1000$ K.

fact, we may estimate the thickening factor F needed to capture the thermal thickness on an LES grid, obtaining $F < k\Delta\delta_L \sim hk/n/\delta_L \sim 1.7$ where n is the number of cells per integral length h and k is the number of cells capturing the steepest temperature rise, typically $n \sim 20$ and $k \sim 3$. The inequality arises for accounting that δ_L is the minimum front thickness corresponding to the undisturbed laminar flame.

Although the non-dimensional numbers listed above are simple estimations, they could suggest that the present flames are in the distributed reaction regime and the intermediate size turbulent structures can disturb and distribute the reaction zone [1,2]. The thickening factor also shows that a typical LES grid captures the thermal front reasonably. The operating conditions, in terms of *Re*, *Ka*, *Da* and *F*, are similar to the (P)PJB [23,24] where ILES, together with complex chemistry, was found adequate. It supports further the choice of ILES for the present simulations.

For the PO and NOP cases, available experimental data include Particle Image Velocimetry (PIV) measurements as well as snapshots of OH-Planar Laser Induced Fluorescence (PLIF) [12–14]. Of course, a total validation of the LES simulations (using detailed chemistry) cannot be done considering solely PIV and OH-PLIF. One would need quantitative measurements of key intermediate species (CO and OH for example) which is very difficult to obtain in a confined burner in presence of particles. Beside PIV and OH-PLIF measurements, semi-quantitative major specie measurements were reported for this case. We have, however, chosen not to use these measurements since our experience has pointed out the difficulties of using advanced measurements data without the active support of the experimentalists.

Instead, one may use a complementary set of data to validate the approach before applying the methodology to the SPRF. Such validation was reported in Ref. [23] showing the potential of the present technique to capture accurately the flow and scalar fields (including OH and CO) in a similar operation, namely reacting jet in the distributed reaction regime. These data support further the use of the present approach and give confidence in the present results – although detailed measurements of OH and CO concentrations are not available.

4. Presentation of the numerical methods and computational study

The CFD code used presently is based on the OpenFOAM object-oriented library [54] and features a reacting low Mach number formulation of equations (1). The spatial discretisation uses an unstructured Finite Volume method [54]. The reconstruction of convective fluxes by central differencing gives second order accuracy in space, and second order accurate backward discretisation is used in time. The convective terms in the scalar equations $(1_{2,4})$ are treated using a Total Variation Diminishing scheme

maintaining high resolution and second order accuracy while preserving boundedness [55]. Time stepping is done implicitly, the pressure–velocity coupling is done with the PISO method [56] and spurious oscillations are avoided using the Rhie-Chow interpolation [57]. A solver strategy, based on judicious blend of conjugate-gradient and multi-grid methods, was used to speed-up the pressure–velocity coupling steps. The equations are solved sequentially using explicit source terms to obtain rapid convergence. A maximum Courant–Fredrich–Levy number of 0.4 is enforced corresponding to a physical time step $\Delta_t \sim 3 \times 10^{-7}$ s. The present settings are well in line with previous works, e.g. [23,46].

The computational domain covers the cylindrical combustor and starts 0.013 m upstream of the injection location, as shown in Fig. 1. Two computational grids were used in the present study. Both body fitted grids consist of unstructured arranged cells, mostly cubic cells. Polyhedral cells are used for body fitting while the wall refinement layers consist of prismatic cells. Local refinements are used along the central jet shear-layer and close to the fuel and air injectors. The high-speed annular air jet nozzle is captured on the finest cells, ensuring that the smaller cells are located where the gradients are expected to be large. On the *medium/fine* grid, 36/48 points are used to describe the outer jet diameter, respectively. The two grids have similar mesh density. The total mesh size was almost doubled and the *medium* grid contains 1.5×10^6 cells compared to 2.9×10^6 on the *fine* grid. In both meshes, the refinements include the nozzle and extend downstream to cover the proximal region of the jet. The region with smaller cells extend down to the middle of the combustor, ensuring an accurate description of the turbulence, shear and reacting layers. We note that the grid resolution tested here are comparable to or finer than the ones usually reported in the literature for reacting jets, e.g. [23,24], and well in line with previous simulations of the SPRF [14]. For the medium grid, we have $F \sim 3\Delta\delta_L \sim 1.7$ indicating that the LES grid resolves reasonably well the reaction front. Table 1 details the simulations performed with the *medium* and *fine* grids.

Table 1
presentation of the ten cases considered.

Case	Mesh	Mode	Walls BC	Mechanism
I	Medium	PO	Adiabatic	J&L [33]
II	Fine	PO	Adiabatic	J&L [33]
III	Medium	PO	Adiabatic	DRM22 [35]
IV	Medium	PO	Adiabatic	Warnatz [36,37]
V	Medium	PO	Wall @1000 K	Warnatz [36,37]
VI	Medium	NPO	Adiabatic	J&L [33]
VII	Fine	NPO	Adiabatic	J&L [33]
VIII	Medium	NPO	Adiabatic	DRM22 [35]
IX	Medium	NPO	Adiabatic	Warnatz [36,37]
X	Medium	NPO	Wall @1000 K	Warnatz [36,37]

Table 2
Inflow boundary conditions for PO and NPO.

		PO	NPO
Operating pressure		101325 Pa	101325 Pa
Annular injector/air	Bulk velocity	121.6 m/s	111.7 m/s
	Temperature	500 K	450 K
	Gas	Methane/air $\Phi = 0.58$	Air
Central jet/fuel supply	Bulk velocity	0 m/s	22.8 m/s
	Temperature	300 K	300 K
	Gas	Methane/air $\Phi = 0.58$	Methane

The boundary conditions (BC) and particularly the inlet conditions are important in the framework of Large Eddy Simulations. One may want to start the computation upstream from the region of interest so that well defined fully developed turbulent flow conditions are used. However, extending the computational domain without decreasing the spatial resolution increases considerably the computational cost. Additionally, in the present combustor (and in many experimental data), the inlet conditions are not fully developed, ideal nor measured. Following [14], we assume flat velocity profiles at the inlets – matching the bulk velocity. Synthetic velocity fluctuations u' are superimposed to the mean fields using random numbers rand in space and time:

$$u'(x, t + \Delta t) = \alpha \cdot u'(x,t) + (1 - \alpha) \cdot \text{TI} \cdot U_{\text{bulk}} \cdot \text{rand}(x,t) \qquad (6)$$

based on the bulk velocity with TI ~ 0.1 and $\alpha = 0.9$. It was verified that the present procedure generates fluctuations that are convected into the combustion chamber. However, it is known that Ji-CoF generates rapidly intense fluctuations and are therefore less sensitive to inflow fluctuations than a jet in coflow [51,52]. It supports the choice of a simple solution as done presently and in [14].

Dirichlet boundary conditions are imposed to model the air and fuel inlets for all scalar variables except the pressure that is modeled as zero-gradient. The air temperature at inflow accounts for preheating and is set to 450 or 500 K [14]. Table 2 lists the operating conditions. The outflow boundary is modeled using flux corrected zero-gradient for velocity, zero gradient for scalars, and a fixed total pressure. Zero-velocity walls are enforced complemented with zero-wall-normal-gradient for the chemical species. Both adiabatic and non-adiabatic walls are considered. In absence of wall temperature measurements, a constant wall temperature of 1000 K is assumed for the non-adiabatic case.

The simulations were started enforcing the PO and NPO boundary conditions and filling the combustor with burnt products. It secured stabilization of the combustion.

Statistical quantities were obtained by averaging over a time-span of at least 2 ms giving about 400τ. No subgrid scale correction was used to compute the Root-Mean-Squared (RMS) fields, i.e. they were computed directly from the resolved quantities. The previous approximation is valid if the resolution is adequate and will be verified by comparing the LES predictions of the RMS fields to experimental data.

Table 1 presents the list of the simulations discussed presented here. The simulations were performed on an AMD6220 (3.0 GHz – 2*8-core nodes) using 32 and 64 cores (medium and fine grid respectively).

5. Results and discussion

5.1. Mean and RMS fields and sensitivity analysis

5.1.1. Grid sensitivity

Fig. 2 shows chosen radial profiles of the axial velocity for both NPO and PO using J&L chemical scheme. As suggested in Fig. 1, the flow features a central jet surrounded by negative axial velocity. The jet penetrates the domain and spreads before turning. The contact between the jet and reverse flow generates relatively strong shear layers with a peak fluctuation intensity up to 20%. The results of the two different grids coincide with slight difference in the mean (less than 3%). The differences are somehow larger for RMS (Root Mean Square) but both grids capture the jet spreading and the peak fluctuation intensity similarly. In fact, increasing the resolution does not enable to resolve more fluctuations. The comparisons presented in Fig. 2 cover only the proximal region of the jet, where the gradients are strongest and fluctuation levels are expected to be highest. However, similar trends are seen further downstream but not shown for conciseness. Plots covering the temperature field (also not presented here) show a similar insensitivity to the choice of the grid, both for mean and RMS. We therefore conclude that the present grid is suitable for LES and the increasing further the resolution would not change the results significantly.
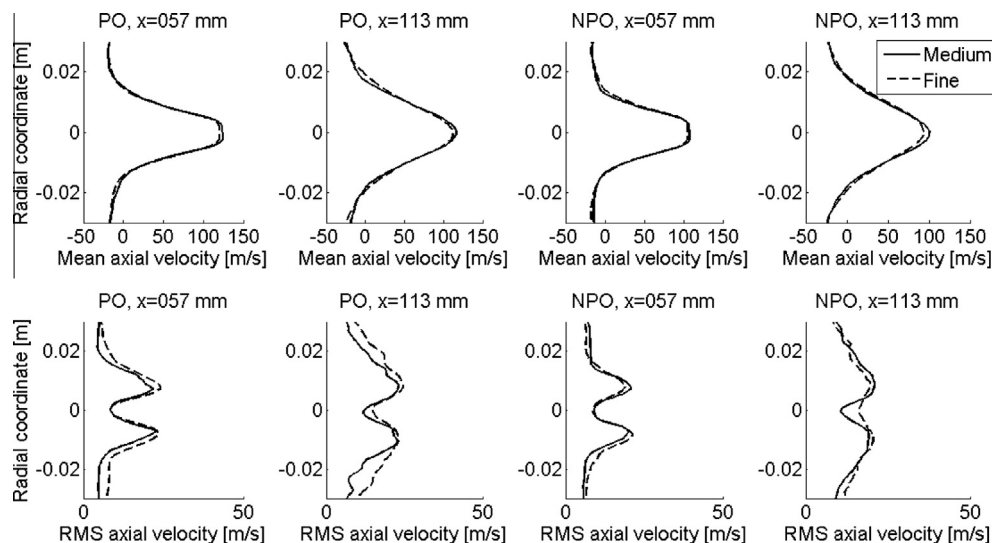

Fig. 2. Mean and RMS of the axial velocity along radial lines using J&L for the PO (left) and NPO (right) cases I and II and VI and VII, respectively. The medium and fine grids are compared.
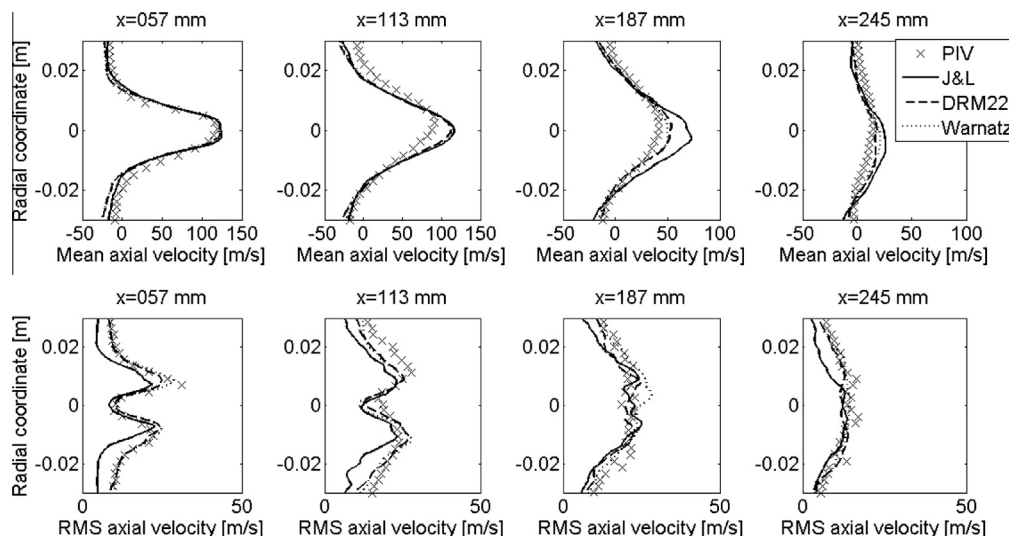
Fig. 3. Mean and RMS of the axial velocity along radial lines for the PO, cases I, III and IV.

5.1.2. Sensitivity to the chemical scheme and comparison with PIV data

A key issue in the simulation of reacting flow is the choice of the chemical scheme describing the reactions. As discussed earlier, there is no established guideline for choosing an adequate mechanism, and we compare several candidates. Fig. 3 shows the radial profiles of the axial velocity during PO, both varying the chemical scheme and comparing with available PIV data [14]. All data sets show the jet penetration, spreading and reverse flow. The shear-layers are identified as peaks in the RMS and agree, in both location and intensity. The discrepancies due to the chemical scheme are not significant for the axial velocity, although the scheme by J&L tends to predict a slightly longer penetration of the jet with a higher peak velocity at $x = 187$ mm. The PIV data show similar physics. At $x = 57$ mm, the agreement is below the experimental uncertainty for the mean velocity field. For the RMS, Warnatz and DRM22 predict levels close to the PIV measurements while J&L underestimates the fluctuation level outside of the shear-layers. At $x = 113$ mm and 187 mm, the PIV profiles show asymmetry while the LES profiles are centered along the axial line. The deviation is visible as a shift in the mean velocity peak – although PIV and LES give a similar profile in terms of shape, spreading and maximum. The RMS levels give again similar profiles. At $x = 187$ mm, both peaks merge giving a single central region with high fluctuation. At $x = 245$ mm, the PIV and LES show an off axis velocity peak. The asymmetry in LES is certainly consequence of the averaging time. However, it only shows in the bottom of the chamber where the dynamics are very slow, as will be shown in the modal analysis. The reaction zone ends prior to this section and it does not add to the present results to continue the averaging longer. In addition, fluctuation levels in this bottom part are well captured by the LES, with agreement below the uncertainty of the measurements.

Fig. 4 complements the previous results with the NPO simulations. Choosing the same axial locations along the chamber, the velocity profiles exhibit the same feature with the velocity peak spreading. The peak amplitudes are slightly lower compared to the PO case, though. The three chemical schemes lead to the same profiles, both means and RMS coincide. The differences with the PIV are more pronounced compared with the PO case with predictions over-estimating the axial velocity at the axis. The spreading of the peak is, however, in agreement with the PIV data. The RMS levels are also close for all data set (excluding the very high values measured at $x = 57$ mm) with differences below the experimental

uncertainty. The influence of the chemical scheme on the velocity field is also limited, except at $x = 245$ mm. From Figs. 3 and 4, one may conclude that the present results capture the flow field in the combustor correctly, both in terms of mean field and fluctuation intensity. In addition, the choice of the chemical scheme does not influence the flow field significantly, although some discrepancies are seen.

In addition to the velocity field, Figs. 5 and 6 report the radial profile of the temperature for cases PO and NPO. Again, the influence of the chemical scheme is investigated. For both cases, the temperature field features a cold jet penetrating the hot gas trapped in the combustor. The location of the temperature gradient coincides with the shear-layer and the peak temperature RMS locations match the regions with high velocity fluctuations. The PO field shows a shorter region with temperature variations with regions around $x = 187$ mm exhibiting a constant temperature and very low fluctuation level. In fact, previous works [14] highlighted the shorter PO reaction zone compared with the corresponding NPO, although their simulations suggest that the temperature radial profile is flat only at $x > 200$ mm. For the NPO, the temperature profile is only flat close to the bottom of the combustor, i.e. $x = 245$ mm. The temperature profiles and fluctuation levels are almost identical when using Warnatz and DRM22. For the PO case, J&L produces comparable results, except for the burnt temperatures that are slightly lower. For the NPO case, the influence of the chemical scheme is not significant in the proximal region ($x = 57$ and 113 mm) but is relatively large at $x = 187$ mm. This location hosts the merging of the two RMS peaks and, as will be evidenced later, features strong heat-release and OH concentration/signal. Differences in modeling the heat-release explain the differences seen in Fig. 6 where it is suggested that J&L over-estimates the burning rate, hence giving higher temperatures at the centerline. The temperature RMS are following accordingly, showing insensitivity in the proximal region and difference thereafter. However, the temperature fields are consistent irrespective of the chemical scheme employed. In fact the resulting influence on the density (hence the flow field) was not shown to be significant. For both the PO and NPO cases, general features of the flame are recovered for all chemical schemes and the sensitivity is limited for the temperature field. It supports the conclusion that, providing that the modeled heat-release rate is reasonable (although not necessarily very accurate), the simulation output will not show significant sensitivity. It opens avenues for using global kinetics for simulating
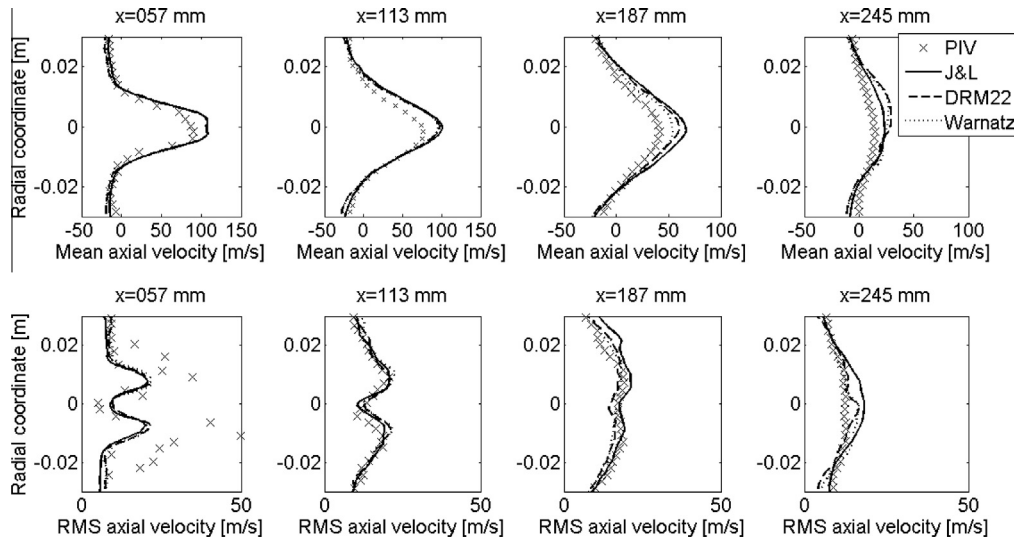
Fig. 4. Mean and RMS of the axial velocity along radial lines for the NPO, cases VI, VIII and IX.
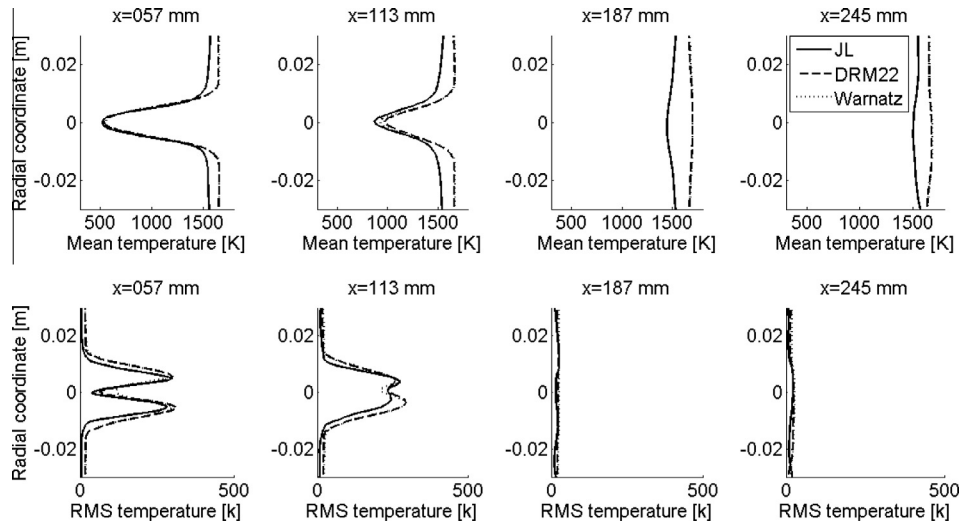

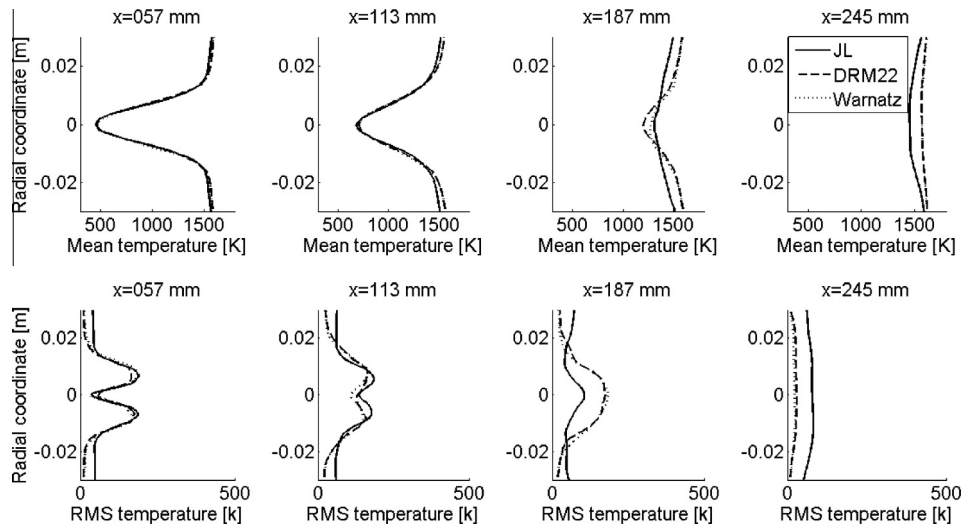**Fig. 5.** Mean and RMS of the temperature along radial lines for the PO, cases I, III and IV.

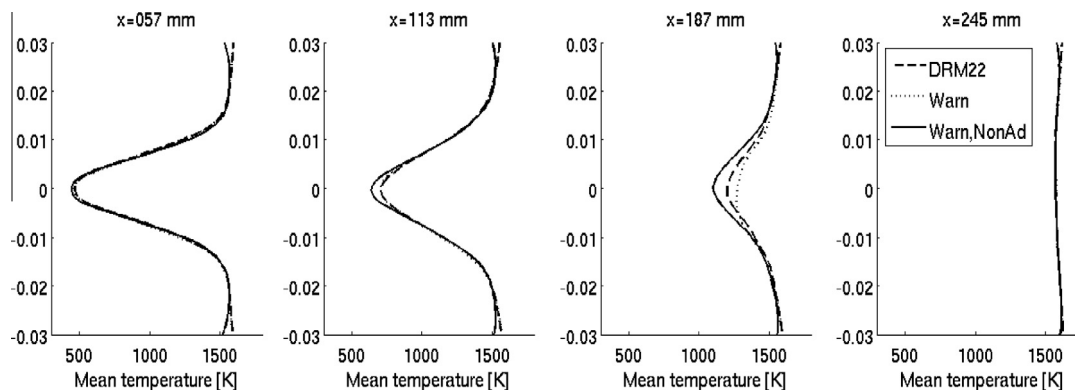**Fig. 6.** Mean and RMS of the temperature along radial lines for the NPO, cases VI, VIII and IX.

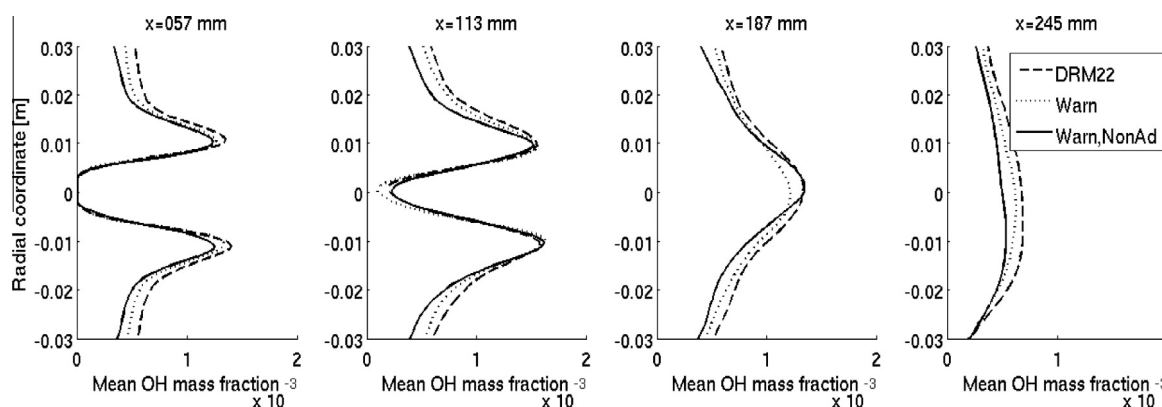**Fig. 7.** Mean temperature along radial lines for the NPO, cases VIII, IX and X.

Fig. 8. Mean of OH mass fraction along radial lines for the NPO, cases VIII, IX and X.

flameless combustion when only general features of the flame (temperature profile for heat-transfer simulations or velocity fields) are of interest. The case when detailed aspects of the flame are of interest is covered in the next section.

5.1.3. Influence of the heat losses and minor species

Minor species are known to be sensitive to the choice of the chemical scheme but also in general to other operating parameters. An important, but often over-looked aspect is the non-adiabatic combustion chamber. Although they are difficult to quantify and often not reported by the experimentalists, the heat-loses at the wall may influence the minor species. In the present work, we include a case imposing a constant temperature at the combustor wall (1000 K), forcing heat-losses in the system. Figs. 7–9 report these results together with varying the chemical scheme for the NPO case. Since we focus on minor species, J&L was omitted in this section. Firstly, Fig. 7 shows the temperature field. The temperature profile evolution follows the pattern described earlier with a jet of fresh cold gas penetrating into the chamber and increasing gradually in temperature. The non-adiabatic simulation shows slightly lower temperatures in the near wall region. The larger temperature difference is seen along the centerline at x = 187 mm. Noticeably, the effect of heat losses is larger than the effect of the chemical scheme, with DRM22 predicting a temperature in between the two simulations using Warnatz's mechanism.

Further, Fig. 8 presents the mean OH mass fraction fields. Firstly, the non-adiabatic effects are seen close to the combustor walls with cooling of the burnt gases giving lower OH concentrations. DRM22 predicts higher OH values in the near wall region compared to Warnatz. The differences are up to 20%. However, the differences

between the two schemes are lower than the impact of the heat losses. In the jet region, the influence of the wall losses and of the chemical scheme are limited for x = 57 and 113 mm. The OH peaks are located in the shear layer and read 0.0015 in all three cases. Further downstream, the differences appear but are limited to ~5%. Again, the effect of non-adiabatic wall is as important as the choice of the chemical scheme. Fig. 9 pursues the investigation reporting the mean formaldehyde mass fraction. Unlike OH which is present in the high temperature regions (often post-flame), formaldehyde appears in low temperature regions and therefore complements OH particularly well. From x = 53 mm to 113 mm, no significant differences are seen between the three cases with peaks in the shear-layer. Formaldehyde is absent from the regions of high temperature hence from the regions most affected by heat losses, explaining the relative insensitivity. At x = 187 mm, the two adiabatic simulations produce the same profile while the heat-losses produce an increase of the formaldehyde but about 30%. This can be explained by the lower temperature at this location (Fig. 7). Hence, the heat-losses cool the burnt gases which are entrained by the reactants and indirectly lower temperature in the reaction zone, favoring the low temperature species, such as formaldehyde.

Regarding the PO cases, Fig. 10 compares the influence of chemical scheme and heat losses on mean temperature and OH. In line with the NPO case, differences are seen close to the wall where heat-losses are more significant. The temperature field is not noticeably affected by the choice of the chemistry. For OH, differences are also seen close to the wall with lower temperatures decreasing the OH level in the post flame zone. The effect of heat-losses on OH in this region is comparable to the effect of changing chemical scheme. The peak OH is less affected by
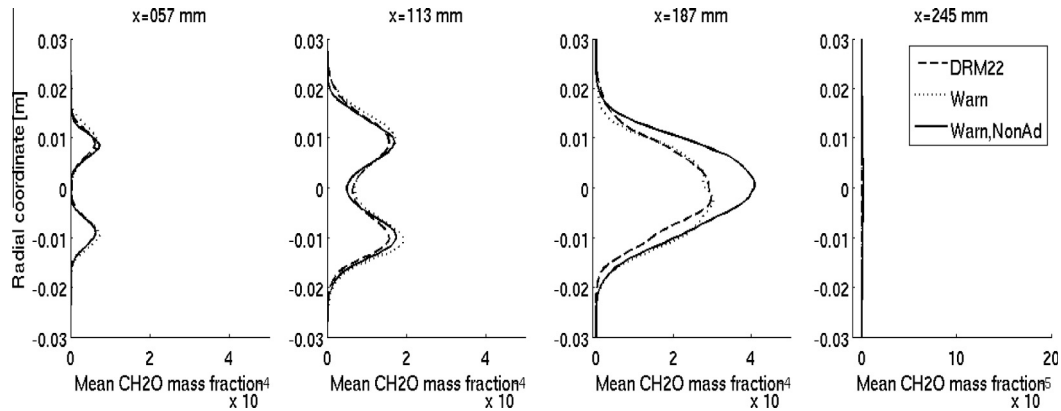
Fig. 9. Mean of CH_2O mass fraction the temperature along radial lines for the NPO, cases VIII, IX and X.
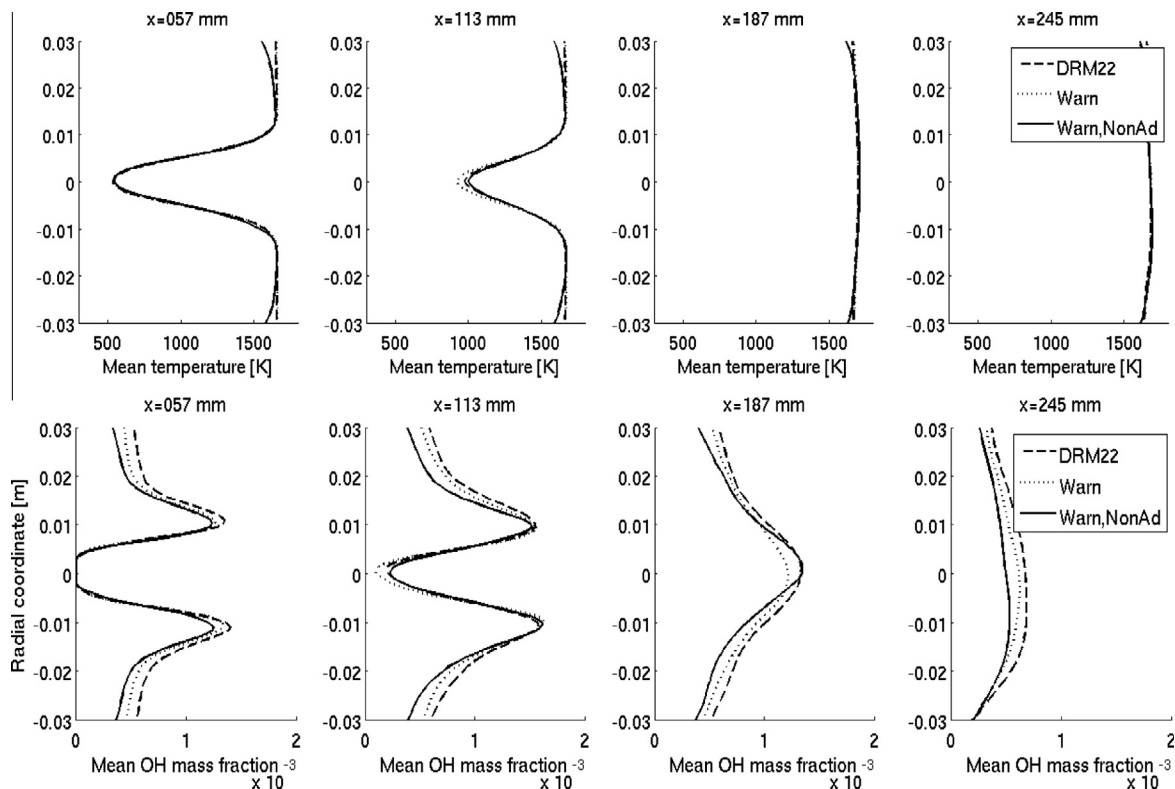

Fig. 10. Mean temperature (top row) and OH mass fraction (bottom row) along radial lines for the PO, cases III, IV and V. Fig. 11: normalized OH mass fraction/signal from LES (IV, IX) and PLIF [13] for PO (right) and NPO (left). Dimensions are given in mm.

heat-losses and DRM22 predicts 5% higher peak OH values compared to Warnatz's mechanism. The location of the peaks (reaction zones), their spreading and merging at $x = 187$ mm is captured similarly by the three simulations. Mean formaldehyde mass fraction profiles indicate not significant differences between the three cases and are therefore not presented. As for the NPO, the choice of chemical reaction scheme affect only marginally the temperature fields while the OH field does not differ by more than 5% between the cases. The heat-losses have a larger effect in the near wall region than the variation of chemical mechanism. However, the major trends of the reaction zone and peak locations are found mainly insensitive.

Based on these results, we select the adiabatic Warnatz simulations (cases IV and IX) for further investigation of the combustion process and examine snapshots in the following section.

5.1.4. Instantaneous fields

Fig. 11 presents randomly chosen snapshots of the OH field/signal comparing the LES results with PLIF results [13]. All cases exhibit a central cold jet surrounded by an OH layer. The OH layer exhibits local maxima and minima. However, one sees a continuous layer delimiting clearly the jet core. This can be explained by the presence of OH in the post-flame zone so even hot but nonreacting parcels show non-zero OH values. In general, the OH field fills a large fraction of the combustor volume. PO and NPO differ in the length and radial size of the jet core (here the central zero OH region). PO presents a thinner core and high OH pockets close to the nozzle exit. For NPO, air exits from the nozzle, and the reaction zone is therefore lifted until fuel can reach the burnt gases/high temperature region (see Fig. 1). This difference is stronger in the LES images. For the PO, the LES underestimates the length of the
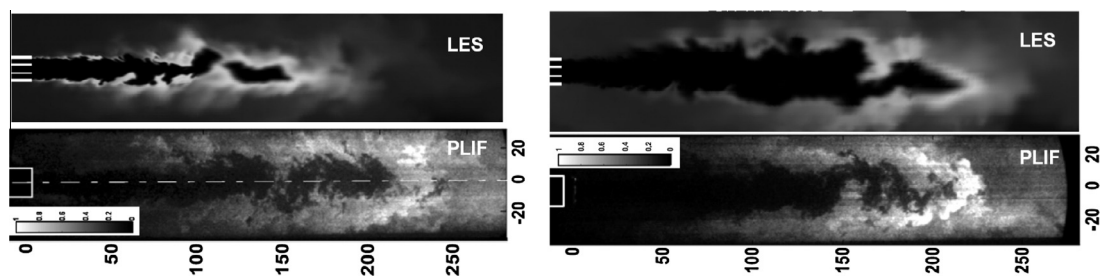
Fig. 11. Normalized OH mass fraction/signal from LES (IV, IX) and PLIF [13] for PO (left) and NPO (right). Dimensions are given in mm.
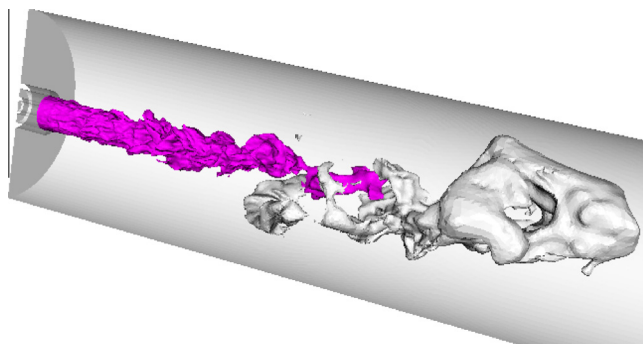

Fig. 12. Iso-surfaces YOH = 0.001 (light-grey) and T = 800 K (blue or grey) from LES (IX). (For interpretation of the references to colour in this figure legend, the reader is referred to the web version of this article.)

Fig. 13. CH_3, CH_2O, CO and OH mass fractions with white iso-line T = 800 K from LES (case IX). Axial dimensions are given in mm.

jet core. The shape of the core is irregular and discontinuous suggesting a 3D shape. For the NPO, the LES predicts similar core length as seen on PLIF data with a jet tip at around x = 220 mm. The shape is also similar on both images with a large core covering the radius range −15 mm to 15 mm. A constriction is seen at x = 150 mm suggesting a 3D (out of plane) shape of the core. In addition to the comparison with the PIV results, the OH fields give confidence that the LES captures the flow dynamics and reaction zone properly.

The instantaneous 3D shape of the jet core and OH iso-surface are further shown in Fig. 12. The jet core is captured using a temperature iso-surface. It follows the shape of the nozzle close to injection with increasing wrinkling with axial location. The wrinkling length scale becomes large enough to provide an off axis motion with a spiral like shape. The high OH region is limited to a region at the tip of the jet core as already seen in Fig. 11. Islands containing high concentrations OH are also seen at locations where the jet core is thin, also in line with evidence in Fig. 11. The high OH regions are distributed non-uniformly around the jet core suggesting large scale motions.

Fig. 13 shows four intermediate species fields at a randomly chosen time step under NPO. The species are chosen to follow the sequence of methane oxidation, namely $CH_4 \rightarrow CH_3 \rightarrow CH_2O \rightarrow CO$ with OH being active in oxidation of CO to CO_2 and remaining in the post flame zone. The zone downstream of the nozzle is not reacting with zero mass fraction of CH_3, CH_2O and CO while OH is low but non zero (i.e. at post flame levels). The reason is the absence of contact of methane with high temperature gas. The NPO configuration forces the lift-off of the reaction zone as only pure air is in contact with the hot gases in the proximal region of the annular jet. While mixing proceeds as one travels downstream, methane is mixed with air and flue gas (as shown in Fig. 1). The low temperature reaction zone (marked by formation of CH_3 then CH_2O) starts at $x \sim 35$ mm downstream of the nozzle. CH_3 develops in the mixing layer following the irregular shape of
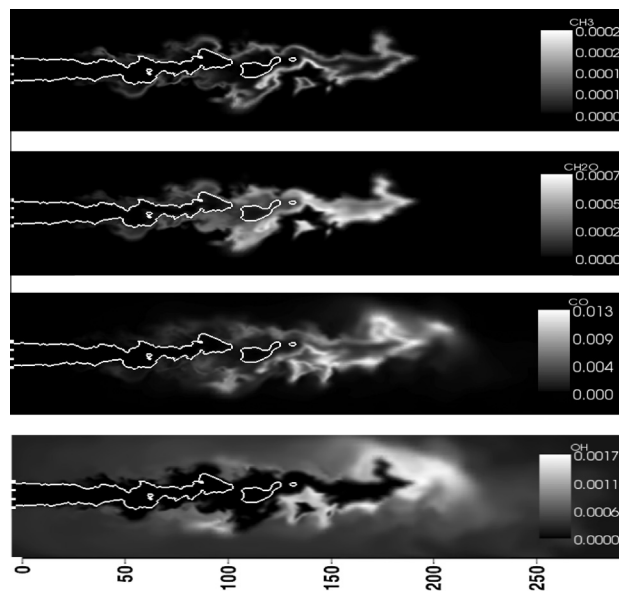
the jet core. The thin CH_3 band is located outward of the jet in the region with temperatures higher than 800 K. Following CH_3, CH_2O features a band of varying thickness, alternating relatively large pockets connected by thinner bands. Unlike CH_3, CH_2O occupies a significant volume in the combustor. CH_3 and CH_2O share the same high temperature limit but CH_2O is present also in the lower temperature range. In fact, CH_2O covers the volume between the iso-line T = 800 K and the CH_3 front. It is, at first glance, surprising since CH_3 precedes CH_2O in the sequence and is expected at lower temperatures. However, unlike CH_3, CH_2O is a stable molecule and may be transported to regions where CH_3 would not be stable. Further OH is found surrounding CH_2O – the low temperature limit of OH and high temperature limit of CH_2O coincide perfectly, well in line with previous experimental observations [11]. The presence of OH on the high temperature side limits the transport of CH_2O toward higher temperatures where it would be converted to HCO. It gives a sharp contour of the CH_2O field delimiting the end of CH_2O and start of OH containing regions. CO lies in between OH and CH_2O as expected since it is generated (not directly) from CH_2O and further reacts with OH. CO levels coincide both with relatively high CH_2O and OH levels, though not simultaneously. The instantaneous CO brush is thick covering up to 10–15 mm which corresponds to the nozzle diameter. The instantaneous CH_2O brush shows the same thickness but unlike CO presents more homogeneous concentration. These brushes evidence the spreading of CH_2O and CO, hence the decrease in peak value as will be quantified later. It is a characteristic feature of

combustion in the distributed reaction regime with thick layers of CO and CH$_2$O resulting from intense turbulent mixing, transporting these intermediates from the production layer toward moderate and high (CO only) temperature regions. Consequently, CO and CH$_2$O are good indicators for identifying the reaction zone location – however, it should be noted that they are not present only in the reaction zone but also upstream (preheat like zone). CH$_3$ is to this respect a better indicator of the low temperature reaction zone. OH complements the picture being present in the high temperature reaction zone (high OH values) and post flame zone (low OH values). The high temperature reaction zone coincides with regions with both OH and CO are present.

Figs. 14 and 15 present instantaneous intermediate specie fields in cross sections for PO and NPO respectively. The axial locations are chosen to ensure a significant heat-release rate. Since the NPO shows heat-release further downstream in the combustor compared to PO, the cut is taken at $x = 65$ mm for PO and $x = 105$ mm for NPO. For PO, the heat-release distribution is not continuous with distinct and elongated pockets/bands concentrating most of the reactions. These pockets have a thickness of ~1.5 mm which is thicker than the corresponding laminar flame. The CO and CH$_2$O field occupy a large fraction of the jet cross section, without direct correlation with heat-release pockets. The CH$_3$ band draws a continuous thick front, coinciding partly with the large heat-release regions. OH is mostly seen outside of the jet and large OH concentrations are seen outside of the high heat-release pockets, mostly in the post-flame zone. The correlation between the four different species is not clear and varies in space – showing the strong influence of turbulence upon the reaction layer.

Similar trends are observed for NPO. However, the levels of intermediate concentration are lower for all species. As a consequence, the peak heat-release is also lower compared to PO, one fourth in the present slice. The NPO present also smoother field with relatively small variation in space compared to PO. The high heat-release regions are also uncorrelated to the scalars. CO, CH$_3$ and CH$_2$O can co-exist with strong heat-release or with no/low heat-release depending on the spatial location. It also shows the influence of turbulence and intermittency on the local structure of the reaction front.

5.1.5. Modal analysis
Fig. 12 suggested the presence of organized large scale structures and we seek to complement the traditional description of turbulent flows (mean and root mean squared (RMS) fluctuation quantities) with statistical quantities describing the nature of the fluctuations. Therefore, we use Proper Orthogonal Decomposition (POD) [58] and project the turbulent flow field on an orthonormal vector base that maximizes the variance content for any subset of the base. Given a vector Q containing the field variables and an orthonormal base b, the expansion reads:

$$Q(x,t) \approx Q^N(x,t) = \sum_{i=0}^{N} a_i(t)b_i(x) \tag{7}$$

where a is the time coefficient associated with the mode b. Note that the approximation Q^N of the turbulence data set Q converges to Q when N goes to infinity and that $i = 0$ corresponds to the time averaged field. Details on the efficient computation of the base b using snapshots are given in the literature [58,59]. A set of 1700 snapshots (collected over ~0.04 s or ~20 flow-through times) was
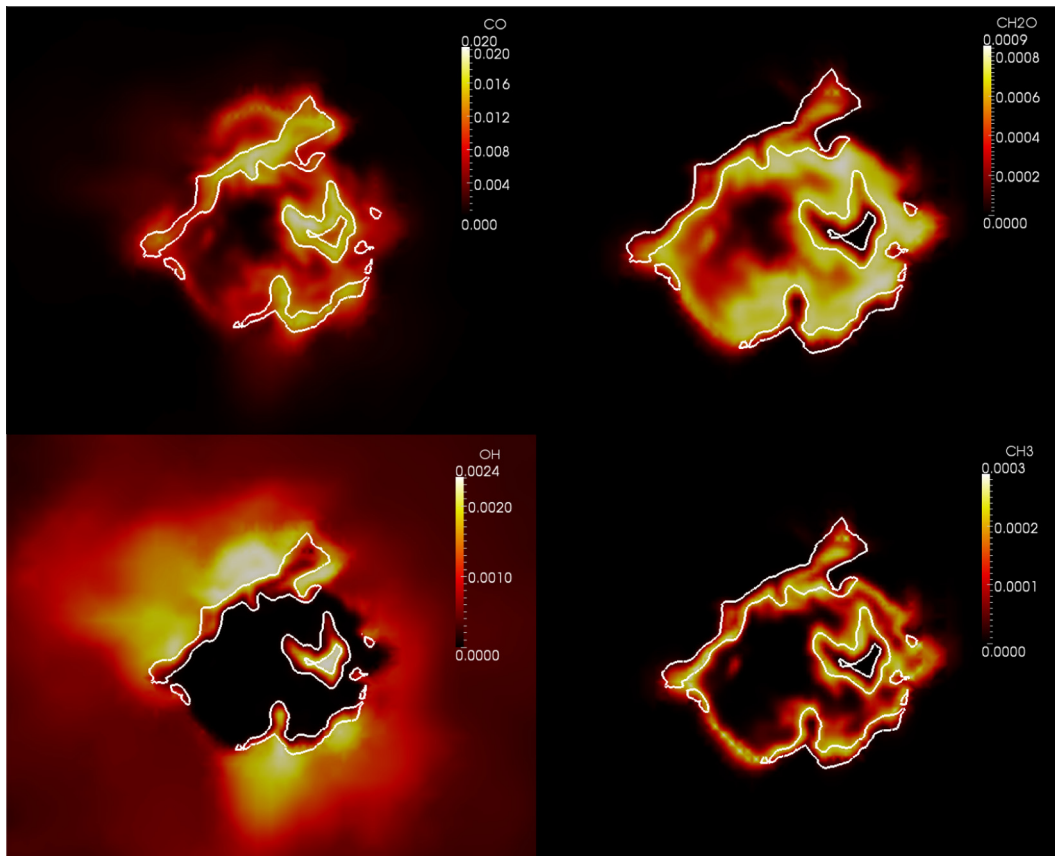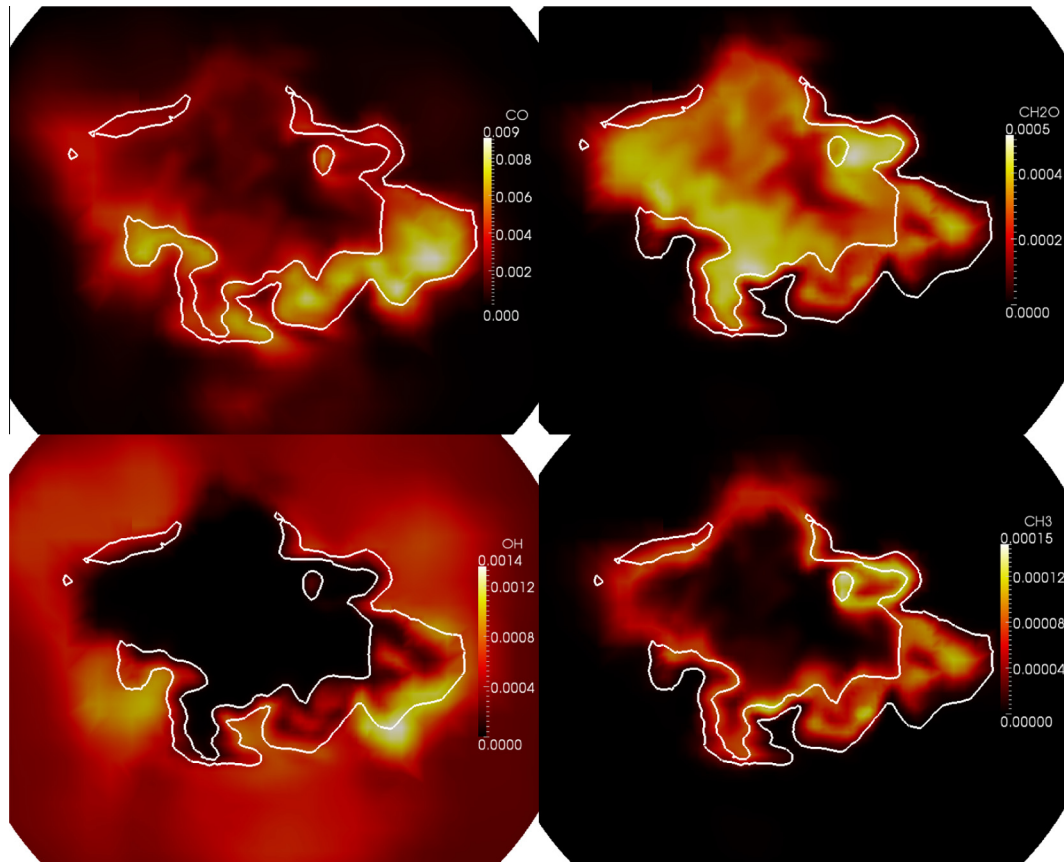

Fig. 14. Instantaneous intermediate species field for PO (case IV) in a cross section ($x = 65$ mm). The heat-release iso-level 4×10^8 W/m^3 (30% of maximum) is shown as white line. The field of view vertical size is 34 mm (y-range [−17 mm, 17 mm]).

Fig. 15. Instantaneous intermediate species field for NPO (case IX) in a cross section (*x* = 105 mm). The heat-release iso-level 1×10^8 W/m^3 (30% of maximum) is shown as white line. The field of view vertical size is 48 mm (*y*-range [−24 mm, 24 mm]).

used for performing the POD upon 2D slices of the temperature field for case IV (PO). The reconstruction of the 3D modes was done as shown by Steinberg et al. [60] or Vuorinen et al. [61]. Further, it has been found that increasing the number of snapshots beyond ~1200 does not influence significantly the first POD modes.

Fig. 16 presents the dominant modes together with an instantaneous snapshot of the temperature field. From the temperature field, we see a sharp gradient just downstream of the nozzle. The temperature increase spreads further downstream increasing the thickness of the temperature front. At $x \sim 30$ mm and $x \sim 55$ mm, the temperature front thickness is about 5 mm (~half of nozzle diameter) but it is thinner in between. The alternating thinner/ thicker temperature front results in the irregular/alternating OH distribution shown in Fig. 11. The temperature front at $x \sim 30$ mm and $x \sim 55$ mm suggests again the presence of organized large scale vortices. These are evidenced with the dominant modes. Mode 1 shows a rotation around the axis resulting in a precession of the jet core. This mode does not show any axial variation and is a pure rotation. Pure rotating modes were already evidenced for JiCoF configurations [52,53] and resemble the present mode 1. Fig. 17 complements the spatial mode with the time coefficient representation in Fourier space. It shows a well-defined peak at ~45 Hz (Strouhal number St ~ 0.0047 based on the air jet outer diameter and bulk velocity). This motion therefore very slow compared to the jet time scale. In fact, the limited time span for collection of the samples impacts on the determination of the slow motion. It prevents determining accurately the peak frequency (broad peak as shown in Fig. 17) but provides an estimate of the low frequency. In addition, the clear spatial coherence of the mode indicates that it is not an artifact of the sampling but a physical mode.

Further, modes 3 and 4 depict a helical mode consisting of a combination of positive and negative contribution – both contributions have the same shape and magnitude and are complementary. The axial wave length is about 25 mm and the modes starts acting in the region $x \sim 40$ mm. The helical shape was already suggested by the temperature field on the top of the figure. with a similar wavelength. Both the rotational and helical motions follow the tip of the cold jet and ends at around $x = 140$ mm. The time coefficient analysis for the helical mode indicates a broad band contribution with a slightly dominant peak at 860 Hz (St ~ 0.09). The helical mode frequency range is therefore slower than what is reported in swirl stabilized flames [58,59] with a larger frequency range.

Fig. 17 also presents the variance content of the different modes. The distribution shows a traditional hyperbolic decrease with increasing mode number. However, the first mode only covers 5% of the total variance. Together, the 5 first modes represent ~20% of the variance content. The rest of the fluctuations are spread into numerous modes with even lower individual content. Again, it differs significantly from swirl stabilized flames which concentrate up to 30% or 40% of the variance into a pair of modes [59]. The difference lies in the combustion regime. Swirl stabilized premixed flames feature a sharp temperature gradient and this thin front is convected and transported by the large scale coherent motions. The flame front is often an order of magnitude thinner than the coherent structures. The resulting temperature fluctuation is therefore strongly linked to the helical mode, explaining the high concentration of variance in few modes. On the contrary, high *Ka* combustion (Figs. 13 and 16) exhibits thick temperature fronts without clear scale separation between large scale coherent structures and combustion. As a result, the helical mode does not only
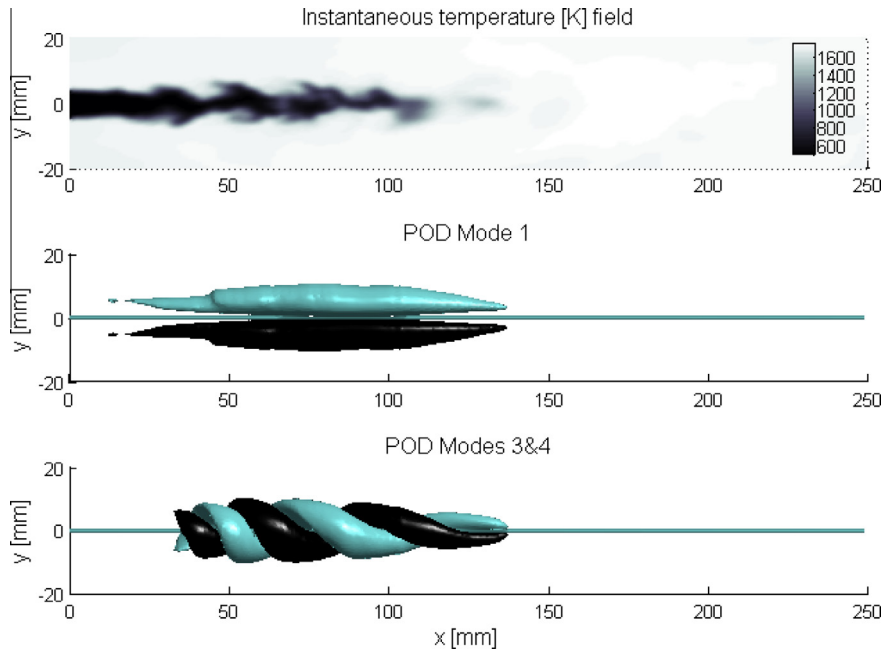
Fig. 16. Instantaneous temperature field and 3D temperature based POD modes for PO (case IV). POD modes are represented as iso-surfaces of positive (black) and negative (grey/cyan) fluctuation. The axis is also evidenced. (For interpretation of the references to colour in this figure legend, the reader is referred to the web version of this article.)
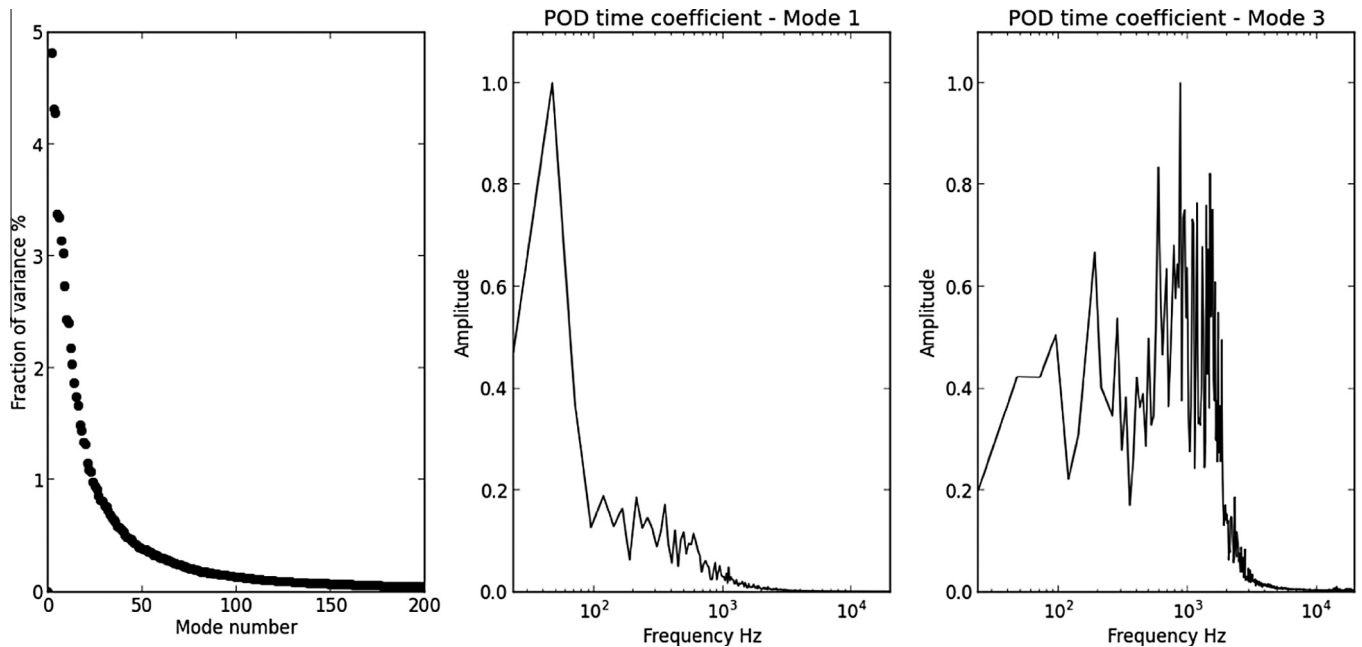

Fig. 17. Variance distribution between POD modes (left) and representation of the POD time coefficients in the Fourier space for modes 1 (center) and 3 (right).

convey the temperature front but can also thicken it – hence reduce the temperature fluctuation. Fig. 16 exemplifies the phenomenon. One can guess the effect of helical mode from the zig–zag shape of the low temperature (dark) region. However, the extremities of the jet core exhibit a thicker temperature front indicating that the helical mode does not only convect the front. It results a distribution/transport of some intermediate species across the reaction layer, as exemplified with CO and CH_2O previously.

5.1.6. Scatter plots and analysis in the compositional space

The interplay of turbulence and chemistry is further examined in the compositional space. Firstly, we examine the mixture

fraction distribution for the NPO (case IX). The axial locations are chosen to be located where intermediate species start to appear (57 mm), at location of large pockets of CH_2O (113 mm) and at the tip of the reaction zone (187 mm), see Fig. 13. Fig. 18 reveals that at $x = 53$ mm, the fluid parcels consist of relatively homogeneous hot gas at $\Phi = 0.58$ while cold gas browses through a wide range of equivalence ratios. The fuel air mixing proceeds still in the cold gases. In between, a relatively wide range of mixture fraction compositions react and exhibit intermediate temperatures. Further downstream at $x = 113$ mm, the mixture fraction is more homogeneous, in particular the cold fuel rich parcels (center of the jet) have already mixed with surrounding air. It remains a
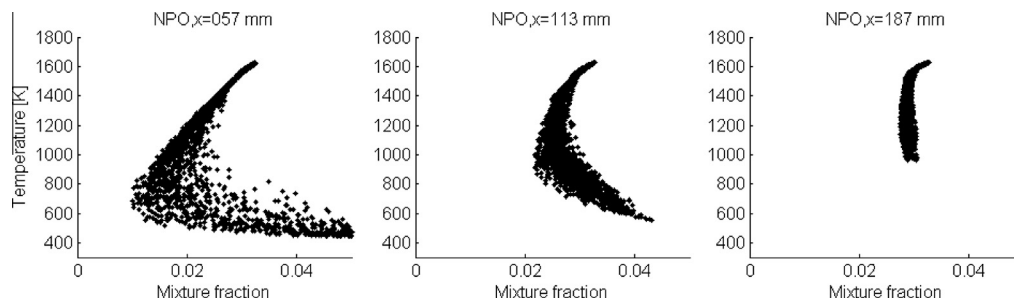
Fig. 18. Scatter plot of temperature in the mixture fraction space collected over three cross-sections at *x* = 57, 113 and 187 mm (case IX).

stratified reactive/reacting mixture. Further at *x* = 187, the fuel/air mixing is complete and the mixture fraction is homogeneous, matching Φ = 0.58. This finding is well in line with early results from the literature [14] reporting that combustion occurs in a pre-mixed stratified mode with rapid premixing upstream of the strong reactions zone (here around *x* = 113 mm).

Further, we examine the CH_2O distribution for both PO and NPO cases. Fig. 19 (top) shows that PO scatter plots follows the envelope closely (laminar freely propagating flame/flamelet at equivalence ratio Φ = 0.58) but extends below. For a fixed temperature, the scatter/departure from the laminar flame profile results from local stretch or interaction with turbulence. Fig. 11 exemplifies such non-homogeneities for OH with local maximums and sudden disappearance of OH peaks. Fig. 19 (bottom) presents similar graphs for NPO. The CH_2O scatter plot presents the same bell shape as the PO or flamelet curve. The maximum is at *T* = 1200 K but the amplitude of CH_2O is dramatically decreased for NPO – a factor 1/4 at *x* = 57 mm and 1/2 at *x* = 113 mm. A large scatter of CH_2O is seen for a fixed temperature, indicating transport of CH_2O across the temperature brush.

Fig. 20 complements these elements showing CO mass fraction in similar scatter plots. For PO, the CO also follows the envelope of the flamelet curve with a maximum in form of a bell shape. However, the scatter is larger than for CH_2O with up to a factor 4 in CO mass fraction at a single temperature. This scatter results from interaction with intense turbulence. For example, the lower values

of CO at *T* = 1300 K result from fluid parcels which are highly diluted with flue gases, hence securing relatively high temperature but low CO levels, hence CO emissions [10]. We note that the scatter plots for PO differ from a traditional laminar premixed flame but are still reminiscent, in particular following the envelope. Fig. 11 showed that the OH front consists of alternating pockets of high and low OH concentrations. This feature explains the scatter below the laminar flame curve. However, the proximity of the flamelet curve suggests similarities between premixed flames and premixed flameless-like combustion. Similar conclusions were drawn from experimental data analysis [11].

For the NPO, CO levels are significantly lower, not reaching more than 50% of the corresponding flamelet/PO value. The fluctuation intensity is, however, also large. For NPO, the reaction zone is located further downstream and the dilution by flue gas is strongly promoted before reaction start. Again the dilution by flue gas decreases the fuel concentration (hence potential CO peak) while it increases the temperature. The NPO shows relatively low intermediate CO and CH_2O instantaneous peak values compared to traditional flames, at equivalent power and temperature. This is a noticeable feature of the distributed reaction regime and well in line with the larger spatial extends of the CO and CH_2O instantaneous brushes. The turbulence mixing distributes differently the intermediate species from the location of production to the regions where they are stable. Unlike PO, NPO departs significantly from the flamelet curve. Fig. 18 established that the premixing is
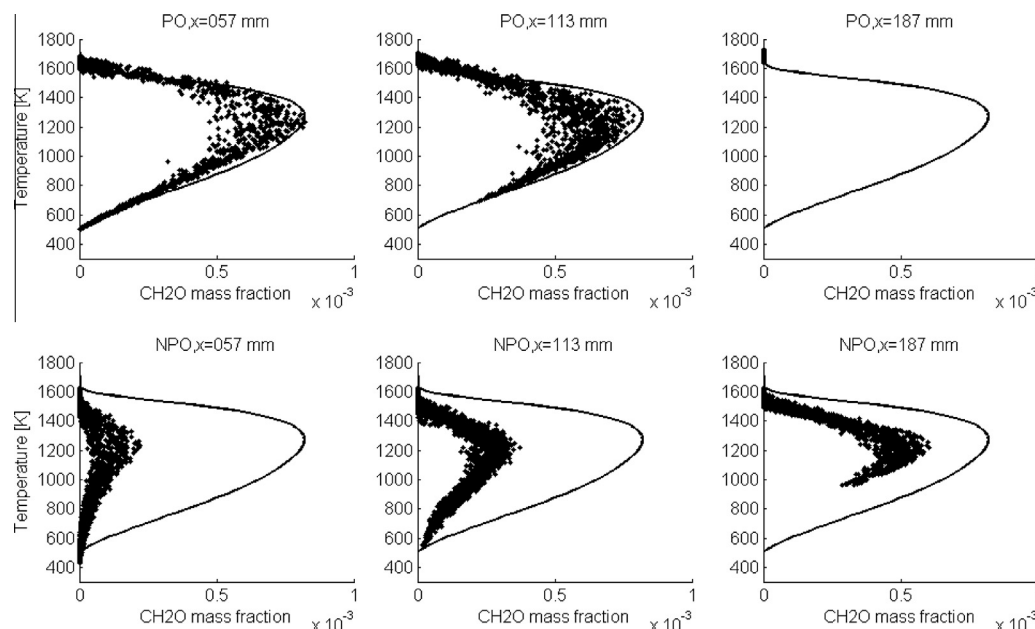

Fig. 19. Scatter plot for cases IV and IX at different axial locations. The continuous line corresponds to a laminar freely propagating flame at equivalence ratio Φ = 0.58.

Fig. 20. Scatter plot for cases IV and IX at different axial locations. The continuous line corresponds to a laminar freely propagating flame at equivalence ratio $\Phi = 0.58$.
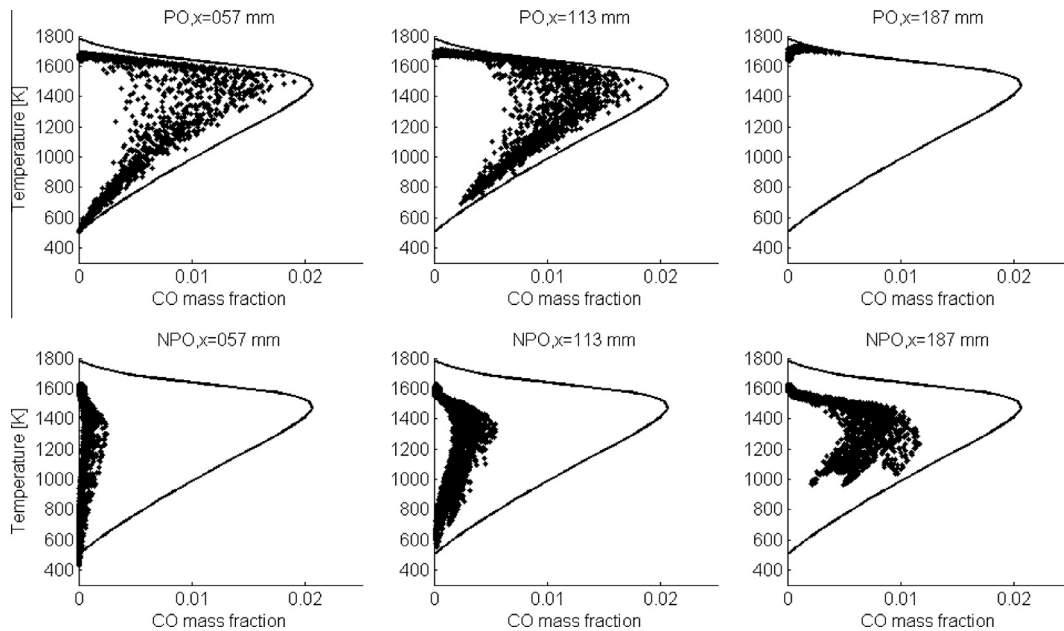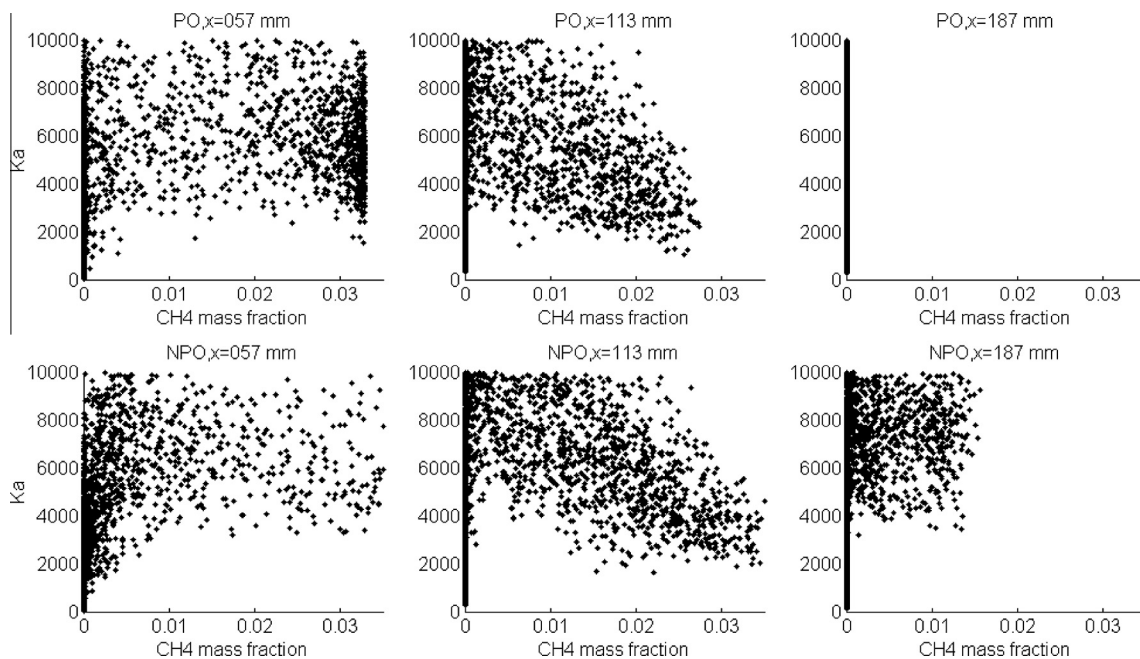

Fig. 21. Scatter plot of the local Karlovitz number in the methane mass fraction space for cases IV and IX at different axial locations.

achieved by $x = 183$ mm so that the strong reaction region ($150 < x < 220$ mm in Fig. 11) operating in the premixed regime. The mixture fraction is homogeneous but the dilution rate with vitiated gases is higher than for PO and explains the lower CO and CH_2O concentrations. In that respect, the NPO configuration has a clear advantage for flameless operation.

The departure from flamelet regime is further quantified by plotting the distribution of the local Ka in the compositional space. Here we choose the methane mass fraction as x-axis. For PO, there is a direct relation between fuel concentration and progress variable, justifying our choice. For NPO, one should follow both the mixture fraction and the mixture. However, the location of the sampling planes is such that the fuel is already mixed with flue

gas and oxidant. For instance, Fig. 18 shows limited variance in mixture fraction and both very lean and very rich parcels are not existing. It suggests that low methane mass fraction correspond to burnt or burning parcel and it is a reasonable indicator of the mixture status in the present case.

As showed in Refs. [23,24], the local values of Ka vary significantly from the average estimation and give a more precise picture of the combustion regime. Fig. 21 presents the distributions as function of the local methane mass fraction. It enables to filter out the events where no fuel is left to burn. Both NPO and PO show a large distribution with Ka varying between 1000 and 10,000. The distributions contain value far above the global estimation. It is due to the over simplification of the global number, not accounting

for the very strong local shear. In fact, the strong variations are consequences of the intermittent behavior and intense turbulence. The reverse flow induces a strong shear that results in very small turbulent structures that penetrate the reaction zone, quantified by Ka above 1000. The trend at $x = 113$ mm is clear with lower Ka values being more represented at higher methane concentrations while high Ka occurs when the fuel concentration has decreased. It follows the aerodynamic of the jet with moderate and low methane corresponding to the reaction zones in the strong shear-layers.

Of course, these estimations are to be taken with care as they rely on the subgrid scale model for estimating the turbulence properties and on laminar quantities for the reaction time scales. It provides though an idea of the combustion regime and here show a large departure from the flamelet or thin flame regime.

6. Summary and conclusions

Although flameless combustion is a promising avenue, the non-linear interaction between chemical reactions and turbulence is not sufficiently understood to design flameless combustors for gas turbine application. This paper contributes with one of the first investigations of the combustion process in the distributed reaction regime (hence in flameless-like mode) using Large Eddy Simulation and complex chemistry.

A comprehensive sensitivity analysis was performed highlighting that the present results are mostly unchanged by refining the grid further. Comparisons with experimental data also support that the grids used presently are sufficiently fine and simulate turbulence levels accurately. It follows that reasonable LES grids, enabling to capture the flow features, are adequate to capture flameless combustion as the reaction zone is typically larger than the mesh spacing. This analysis also compared several chemical mechanisms. If the global mechanisms predict the heat-release reasonably, larger mechanisms are required to capture the intermediate species. For that point, we have compared a skeletal mechanism (DRM22) with a more complete mechanism by Warnatz. The predictions are comparable with relatively small differences in intermediate species predictions – the peaks are at identical locations but differ slightly in magnitude. The influence of the heat-losses upon the results is, however, larger. The predictions of OH are indeed more sensitive to the heat losses than to the choice of the chemical mechanism. CH_2O levels are, however, much less sensitive to either the heat-losses or the mechanism. Heat-losses at the wall are often disregarded by experimentalists and not reported in articles. We hope that the growing reporting of the influence of this parameter will encourage the community to include an estimation of the heat-losses in the operating parameter list.

Based on the detailed chemistry simulation results, the coherent structures were extracted by modal analysis. The flow dynamics exhibit large scale rotation of the jet (processing jet) as well as a helical motion. The latter is responsible for the zigzag-like shape of the jet core when observed in a 2D longitudinal plane. In this study, we used the temperature field as base for the modal analysis. We report a relatively flat distribution of variance content, which is different from that for traditional flames. In fact the dominant modes only account for 20% of the total temperature fluctuation. It is explained by the relatively thick temperature gradient which smooths the temperature fluctuation induced by the flow features.

Focusing on the several intermediate species, it was found that the non-premixed operation is closer to flameless operation with spatially distributed and low maximum value of intermediate fields (CH_2O and CO). In fact, the CH_2O and CO distribution covers significant fractions of the combustor. This point is of interest for

experimentalists who wish to identify the distributed reaction regime, in particular in systems where the distributed reaction regime co-exists intermittently with traditional flames. Our recommendation would be to monitor simultaneously CH_2O and CH_3 (qualitative measurements would be enough) and identify the region where CH_2O extends significantly toward lower temperatures.

Finally, the NPO configuration was found more advantageous for flameless operation as it naturally allows entrainment of flue gas by air (hence without reaction) and larger dilution (compared to PO) as well as near complete premixing before combustion. These advantages are not solely seen in term of reducing CO or NO_x emissions. The propensity to undergo thermo-acoustic instabilities and the fluctuation levels associated with these depends on the heat-release rate. The NPO shows lower heat-release rate per unit volume, which is also more distributed in the combustor volume – together it suggests better stability and more silent combustion. Of course, a word of caution is needed here since the present combustor is not operated at power densities comparable to industrial gas turbine or aero-engines. There is therefore some further experimental work required for making this design an industrial burner.

Acknowledgments

References

[1] Bilger RW, Pope SB, Bray KNC, Driscoll JF. Paradigms in turbulent combustion research. Proc Combust Inst 2005;30:21–42.

[2] Poinsot T, Veynante D. Theoretical and numerical combustion. 1st ed. Philadelphia: RT Edwards; 2001.

[3] Wunning JA, Wunning JG. Flameless oxidation to reduce thermal no-formation. Prog Energy Combust Sci 1997;23:81–94.

[4] Katsuki M, Hasegawa T. The science and technology of combustion in highly preheated air. Proc Combust Inst 1998;27:3135–46.

[5] Cavaliere A, de Joannon M. MILD combustion. Prog Energy Combust Sci 2004;30:329–66.

[6] Weinberg F. Heat-recirculation burners: principle and recent developments. Combust Sci Technol 1996;121:3–22.

[7] Weber R, Verlaan AL, Orsino S, Lallemant N. On emerging furnace design methodology that provides substantial energy savings and drastic reductions in CO_2, CO and NO_x emissions. J Inst Energy 1999;72:77–83.

[8] Mortberg M, Blasiak W, Gupta AK. Combustion of normal and low calorific fuels in high temperature and oxygen deficient environment. Combust Sci Technol 2006;178:1345–72.

[9] Szego GG, Dally BB, Nathan GJ. Operational characteristics of a parallel jet MILD combustion burner system. Combust Flame 2009;156:429–38.

[10] Duwig C, Stankovic D, Fuchs L, Li G, Gutmark E. Experimental and numerical study of flameless combustion in a model gas turbine combustor. Combust Sci Technol 2008;180:279–95.

[11] Duwig C, Li B, Li ZS, Aldén M. High resolution imaging of flameless and distributed turbulent combustion. Combust Flame 2012;159–1:306–16.

[12] Bobba MK, Gopalakrishnan P, Periagaram K, Seitzman JM. Flame structure and stabilization mechanisms in a stagnation point reverse flow combustor. J Eng Gas Turbul Power 2008;130–3. 031505-1-8.

[13] Gopalakrishnan P, Bobba MK, Seitzman JM. LES of premixed and non-premixed combustion in a stagnation point reverse flow combustor. Proc Combust Inst 2007;31:3401–8.

[14] Undapalli S, Srinivasan S, Menon S. LES of premixed and non-premixed combustion in a stagnation point reverse flow combustor. Proc Combust Inst 2009;32–1:1537–44.

[15] Lueckerath R, Meier W, Aigner M. FLOX® combustion at high pressures with different fuel compositions. J Eng Gas Turbul Power 2008;130. 011505-1-011505-7.

[16] Cabra R, Myhrvold T, Chen JY, Dibble RW, Karpetis AN, Barlow RS. Simultaneous laser Raman–Rayleigh–LIF measurements and numerical modeling results of a lifted H2/N2 jet flame in a vitiated co-flow. Proc Combust Inst 2003;29:1881–8.

[17] Gordon RL, Masri AR, Mastorakos E. Simultaneous Rayleigh temperature, OH– and CH$_2$O–LIF imaging of methane jets in a vitiated coflow. Combust Flame 2008;155:181–95.

[18] Oldenhof E, Tummers MJ, van Veen EH, Roekaerts DJEM. Role of entrainment in the stabilisation of jet-in-hot-coflow flames. Combust Flame 2010;157-6:1167–78.

[19] Dally BB, Karpetis AN, Barlow RS. Structure of turbulent nonpremixed jet flames in hot dilute coflow. Proc Combust Inst 2003;29:1147–54.

[20] Medwell PR, Kalt PAM, Dally BB. Imaging of diluted turbulent ethylene flames stabilized on a jet in hot coflow (JHC) burner. Combust Flame 2008;152-1:100–13.

[21] Dunn MJ, Masri AR, Bilger RW. A new piloted premixed jet burner to study strong finite-rate chemistry effect. Combust Flame 2007;151:46–60.

[22] Dunn MJ, Masri AR, Bilger RW, Barlow RS, Wang GH. The compositional structure of highly turbulent piloted premixed flames issuing into a hot coflow. Proc Combust Inst 2009;32:1779–86.

[23] Duwig C, Nogenmyr K-J, Chan CK, Dunn MJ. Large Eddy Simulations of a piloted lean premix jet flame using finite-rate chemistry. Combust Theory Mod. 2011;15-4:537–68.

[24] Duwig C, Dunn MJ. Large eddy simulation of a premixed jet flame stabilized by a vitiated co-flow: evaluation of auto-ignition tabulated chemistry. Combust Flame 2012 [in press].

[25] Sen BA, Menon S. Linear eddy mixing based tabulation and artificial neural networks for Large Eddy Simulations of turbulent flames. Combust Flame 2010;157:62–74.

[26] Raman S, Pitsch H. A consistent LES/filtered-density function formulation for the simulation of turbulent flames with detailed chemistry. Proc Combust Inst 2007;31:1711–9.

[27] Maas U, Pope SB. Simplifying chemical kinetics: intrinsic low-dimensional manifolds in composition space. Combust Flame 1992;88:239–64.

[28] Gicquel O, Darabiha N, Thévenin D. Laminar premixed hydrogen/air counterflow flame simulations using flame prolongation of ILDM with differential diffusion. Proc Combust Inst 2000;28:1901–8.

[29] VanOijen JA, Lammers FA, DeGoey LPH. Modeling of complex premixed burner systems by using flamelet-generated manifolds. Combust Flame 2001;127:2124–434.

[30] Nguyen PD, Vervisch L, Subramanian V, Domingo P. Multidimensional flamelet-generated manifolds for partially premixed combustion. Combust Flame 2010;157-1:43–61.

[31] Duwig C, Fuchs L. Large Eddy Simulation of a H2/N2 lifted flame in a vitiated co-flow. Combust Sci Technol 2008;180:453–80.

[32] Fiorina B, Baron R, Gicquel O, Thevenin D, Carpentier S, Darabiha N. Modelling non-adiabatic partially premixed flames using flame-prolongation of ILDM. Combust Theory Modell 2003;7-3:449–70.

[33] Jones WP, Lindstedt RP. Global reaction schemes for hydrocarbon combustion. Combust Flame 1988;73:233–49.

[34] Galletti C, Parente A, Tognotti L. Numerical and experimental investigation of a mild combustion burner. Combust Flame 2007;151:649–64.

[35] Kazakov A, Frenklach M. Reduced reaction sets based on GRI-Mech 1.2, 1994. <http://www.me.berkeley.edu/drm/>.

[36] Karbach V, Warnatz J. In: Proceedings of the third international workshop on measurement and computation of turbulent non premixed flames, Boulder, CO, 1998. <http://www2.galcit.caltech.edu/EDL/mechanisms/mechs/schultz/warnatz/warnatz.mech>.

[37] Warnatz J, Maas U, Dibble R. Combustion – physical and chemical fundamentals, modeling and simulation, experiments, pollutant formation. 4th ed. Springer; 2006.

[38] Christo FC, Dally BB. Modeling turbulent reacting jets issuing into a hot and diluted coflow. Combust Flame 2005;142:117–29.

[39] Galletti C, Parente A, Derudi M, Rota R, Tognotti L. Numerical and experimental analysis of NO emissions from a lab-scale burner fed with hydrogen-enriched fuels and operating in MILD combustion. Int J Hydrogen Energy 2009;34:8339–51.

[40] Aminian J, Galletti C, Shahhosseini S, Tognotti L. Numerical Investigation of a MILD combustion burner: analysis of mixing field, chemical kinetics and turbulence-chemistry interaction. Flow Turbul Combust 2012;88:597–623.

[41] Smith GP, Golden DM, Frenklach M, Moriarty NW, Eiteneer B, Goldenberg M, Bowman CT, Hanson RK, Song S, Gardiner Jr WC, Lissianski VV, Qin Z, GRI 3.0. <http://www.me.berkeley.edu/gri_mech/>.

[42] Cantera object-oriented software for reacting flows. <http://www.cantera.org>.

[43] Grinstein FF, Kailasanath KK. Three dimensional numerical simulations of unsteady reactive square jets. Combust Flame 1994;100:2–10.

[44] Colin O, Ducros F, Veynante D, Poinsot T. A thickened flame model for Large Eddy Simulation of turbulent premixed combustion. Phys Fluids 2000;12-7:1843–63.

[45] Pitsch H, Duchamp de Lageneste L. Large-Eddy Simulation of premixed turbulent combustion using a level-set approach. Proc Combust Inst 2003;29:2001–8.

[46] Duwig C, Fureby C. Large Eddy Simulation of unsteady lean stratified premixed combustion. Combust Flame 2007;151-1–2:85–103.

[47] Giacomazzi E, Battaglia V, Bruno C. The coupling of turbulence and chemistry in a premixed bluff-body flame as studied by LES. Combust Flame 2004;134-4:320–35.

[48] Chomiak J, Karlsson A. Flame lift off in diesel sprays. Proc Combust Inst 1996;26:2557–64.

[49] Fedina E, Fureby C. A comparative study of flamelet and finite rate chemistry LES for an axisymmetric dump combustor. J Turbul 2011;12–24:1–20.

[50] Jones WP, Prasad VN. LES-pdf simulation of a spark ignited turbulent methane jet. Proc Combust Inst 2011;33–1:1355–63.

[51] Ihme M, See YC. LES flamelet modeling of a three-stream MILD combustor: analysis of flame sensitivity to scalar inflow conditions. Proc Combust Inst 2011;33:1309–17.

[52] Bernero S, Fiedler HE. Application of particle image velocimetry and proper orthogonal decomposition to the study of a jet in a counterflow. Exp Fluids 2000;29–1:274–81.

[53] Duwig C, Revstedt J. Large scale dynamics of a jet in counter flow. In: Eckhardt, editor. Advances in turbulence XII. Springer; 2009. p. 321–4.

[54] Weller HG, Tabor G, Jasak H, Fureby C. A tensorial approach to CFD using object oriented techniques. Comput Phys 1998;12–6:620–31.

[55] Sweby PK. High resolution schemes using flux limiters for hyperbolic conservation laws. SIAM J Numer Anal 1984;21:995–1011.

[56] Issa RI. Solution of the implicitly discretised fluid flow equations by operator splitting. J Comput Phys 1986;62:40–65.

[57] Rhie CM, Chow WL. A numerical study of the turbulent flow past an isolated airfoil with trailing edge separation. AIAA J 1983;21:1525–32.

[58] Berkooz G, Holmes P, Lumley JL. The proper orthogonal decomposition in the analysis of turbulent flows. Annu Rev Fluid Mech 1993;25:539–75.

[59] Iudiciani P, Duwig C. Large Eddy Simulation of the sensitivity of vortex breakdown and flame stabilisation to axial forcing. Flow Turbul Combust 2011;86–3:639–66.

[60] Steinberg A, Boxx I, Stöhr M, Meier W, Campbell C. Effects of flow structure dynamics on thermoacoustic instabilities in swirl-stabilized combustion. AIAA J 2012;50:952–67.

[61] Vuorinen V, Yu J, Tirunagari S, Kaario O, Larmi M, Duwig C, et al. Large-Eddy Simulation of highly underexpanded transient gas jets. Phys Fluids 2013;25–1:016101.